EXPERIMENTAL ANALYSIS AND VALIDATION OF ULTRASONIC TORSIONAL WAVES

ULTRASONICS LAB
TISSUE MECHANICS

EXPERIMENTAL ANALYSIS AND VALIDATION OF ULTRASONIC TORSIONAL WAVES

author:
INAS H. FARIS

supervisor:
GUILLERMO RUS CARLBORG

May 2021

A DISSERTATION SUBMITTED IN PARTIAL FULFILLMENT OF THE REQUIREMENTS FOR THE DEGREE OF DOCTOR OF PHILOSOPHY

Doctoral Programme in Civil Engineering
Department of Structural Mechanics and Hydraulic Engineering
University of Granada
Granada (Spain)

UNIVERSIDAD DE GRANADA

Editor: Universidad de Granada. Tesis Doctorales
Autor: Inas H. Faris
ISBN: 978-84-1306-972-2
URI: http://hdl.handle.net/10481/69872

"Nothing in life is to be feared; it is only to be understood."

Marie Curie

Acknowledgements

My deep gratitude goes first to my supervisor, Prof. Guillermo Rus. Who expertly guided me through this part of my postgraduate stage and shared the excitement of nearly four years of discovery. His unwavering enthusiasm for physics and engineering kept me constantly engaged with my research. His generosity made my time at the Ultrasonic Lab enjoyable.
I spent countless days observing Guillermo, with lots of fascination and magic, when he programs, configures and measures all kinds of things he encounters. This picture of his made me, after a lifetime, discover what I really want to do. He makes me have big dreams.

My appreciation also extends to my laboratory colleagues. Antonio and Jorge's mentoring and encouragement have been precious; their early insights launched the greater part of this dissertation. Many thanks also to Jose, Bea, Juanma and Manu, who enlivened the -3 subbasement with good humour, engineering, music, some remarkable disastrous experiments that we have carried out well due to the episodes of laughter they caused. They all succeed in creating a positive atmosphere in which to do science.

Notable credits go to *the millionaires*, the *coffee tigers*, the *evil one and his enemy*, Lucia and Esther for their love and patience. Because they always understood.

I am indebted to my family, whose value for me only grows with time.

Inas

Sometimes my courage fails me and I think I ought to stop working, live in the country and devote myself to gardening[1]. But I am held by a thousand bonds, and I don't know when I shall be able to arrange things otherwise. ***Nor do I know whether, even by writing scientific books, I could live without the laboratory.***[2]

[1] A bakery in Órgiva, in my case
[2] Letter to her sister Bronya, September 1927. In Eve Curie, Madame Curie (1938).

Publications & Conference presentations

Publications

- **Faris IH**, Melchor J, Callejas A, Torres J, Rus G. Viscoelastic Biomarkers of Ex Vivo Liver Samples via Torsional Wave Elastography. Diagnostics (Basel). 2020;10(2):111. Published 2020 Feb 19. `doi:10.3390/diagnostics10020111`
- Callejas A, Melchor J, **Faris IH**, Rus G. Hyperelastic Ex Vivo Cervical Tissue Mechanical Characterization. Sensors. 2020; 20(16):4362. `https://doi.org/10.3390/s20164362`
- Rus G, **Faris IH**, Torres J, Callejas A, Melchor J. Why Are Viscosity and Nonlinearity Bound to Make an Impact in Clinical Elastographic Diagnosis? Sensors. 2020; 20(8):2379. `https://doi.org/10.3390/s20082379`
- Callejas A, Melchor J, Faris IH, Rus G. Hyperelastic Ex Vivo Cervical Tissue Mechanical Characterization. Sensors. 2020; 20(16):4362. `https://doi.org/10.3390/s20164362`
- Jorge Torres, **Inas Faris**, Antonio Callejas, "Histobiomechanical Remodeling of the Cervix during Pregnancy: Proposed Framework", Mathematical Problems in Engineering, vol. 2019, Article ID 5957432, 11 pages, 2019. `https://doi.org/10.1155/2019/5957432`
- Callejas A, Gomez A, **Faris IH**, Melchor J, Rus G. Kelvin–Voigt Parameters Reconstruction of Cervical Tissue-Mimicking Phantoms Using Torsional Wave Elastography. Sensors. 2019; 19(15):3281. `https://doi.org/10.3390/s19153281`
- Yazdi, A. A., Melchor, J., Torres, J., **Faris, I.**, Callejas, A., Gonzalez-Andrades, M., & Rus, G. (2020). Characterization of non-linear mechanical behavior of the cornea. Scientific RepoRtS, 10(1), 1-10.

Conference presentations

- Ex vivo human cervix acoustical shear ultrasonic properties, International Congress on Ultrasonics, Brugge (Belgium),2019, INAS H FARIS; Antonio Manuel Callejas Zafra; Jorge Torres Perez; Juan Manuel Melchor Rodríguez; Guillermo Rus Carlborg.
- Assessment of mechanical biomarkers of ex-vivo liver samples, 27th International Conference on Composites or Nano Engineering, University of Granada, Granada (Spain), 2019, INAS H FARIS; Antonio Manuel Callejas Zafra, Guillermo Rus.
- Acoustical biomechanical properties of ex-vivo human cervix, Euroson, Granada (Spain), 2019, INAS H FARIS; Antonio Manuel Callejas Zafra; Jorge Torres Perez; Juan Manuel Melchor Rodríguez; Guillermo Rus Carlborg.
- Mechanical biomarkers by torsional wave elastography for gestational diagnosis, First Colloquium of The Spanish Theoretical and Applied Mechanics Society, Madrid (Spain)2019, INAS H FARIS; Antonio Manuel Callejas Zafra; Juan Manuel Melchor Rodríguez; Jorge Torres Perez; Guillermo Rus Carlborg.
- Propiedades ultrasónicas del cizallamiento acústico de muestras ex vivo de hígado animal, VIII Reunión del Capítulo Nacional de la Sociedad Europea de Biomecánica, Castellón (Spain), 2018, INAS H FARIS; A Callejas, Juan Manuel Melchor Rodríguez; Guillermo Rus Carlborg.
- Experimental analysis and validation of cervical tissue biomechanical properties using SWE. The World Congress of Biomechanics, Dublin (Ireland) 2018, INAS H FARIS; Juan Manuel Melchor Rodríguez; Guillermo Rus Carlborg; Antonio Manuel Callejas Zafra.

Abstract

The structural microarchitecture of soft tissue is getting attention among the biomechanical engineering community and rising interest in clinical diagnosis in a broad spectrum of specialities. The new scientific concept of torsional wave ultrasound will enable the in vivo and noninvasive quantification of a new class of biomarkers. These biomarkers, which are direct measures of tissue mechanical properties, are intimately related to the structural microarchitecture of soft tissue and ideal for diagnostic applications. This vision will be enabled by the unique technology proposed here that generates and senses torsional waves in tissue. The breakthrough that this new generation of physical-mechanical biomarkers implies will have a long-term impact. The elastic functionality of tissues is intimately linked to a variety of pathologies. Its quantitative measurement in vivo constitutes a disruptively new diagnostic principle proposed only recently. Well beyond birth and labour disorders (prematurity, induction failures, placenta, etc.), it has enormous potential of being extended to diagnose a growing range of highly prevalent pathologies, including solid tumours (e.g. prostate, cervix, breast,melanoma), connective tissue disorders (ligament injuries, ageing disorders), and liver fibrosis, to name a few. Quantifying the elastic functionality of the cervix is currently not a standard diagnostic tool since no elasticity quantifying technologies exist currently or are still under early research. One of the most important potential torsional wave device applications will reduce infant mortality and childhood morbidity. By quantifying biomechanical properties of the cervix in at-risk women, sufficiently early detection of preterm birth may be identified so that suitable interventions can be implemented to delay birth. The noninvasive in vivo quantification of the biomechanical properties of the cervix will be the clinical focus of this project. This will be accomplished by combining the underlying theory, the technological advances necessary for a proof-of-concept torsional wave diagnostic probe, and model-based inverse algorithms to reconstruct the cervical stroma microarchitecture to predict its elastic evolution, and hence predict its structural ability to dilate. Finally, and most importantly, this project broadens the scope of applications, paving the way to any situation related to modifications of the collagen mechanics, like mechanobiological cell signalling, controlling tumour growth, inflammatory and healing processes, etc., and opening a new and broad field of research with impacting applications.

The research group to which I belong has developed the torsion wave elastography technique and has patented an isotropic sensor that has been validated in vivo by measuring under different conditions (pressure and angle of incidence) in pregnant women and non-pregnant volunteers. At the same time, the validation was done against a rheometer with ex vivo tissue samples. My contribution to the work focuses on validating the sensor against the gold standard: shear wave elastography using a 256-channel verasonics vantage system. The validation was concentrated at the beginning employing tissue-mimicking phantoms, animal tissue; liver, and breast. When the SWE technique was managed, I focused on ex vivo samples of the human uterine cervix due to the difficulty of obtaining these samples. Viscoelastic biomarkers were determined from cervical tissue by fitting four rheological models. As far as we know, these results asre the only values that have been presented using this technique. an additional step was to explore how does the sensor behave by measuring tissues consisting of several layers, ie: epithelial and conective. Being the fist much thinner than the second. Therefore, to check the type of waves propagating in shell-like elements, a new sensor was designed to measure corneas and have a concave shape. The torsion wave elastography technique could detect tissue changes due to pathology/damage and was equally validated against shear wave elastography and tensile machine tests. The results agree pretty well. Another contribution is to investigate soft tissue anisotropy by designing and programming validation experiments of a sectorized torsion wave sensor with three channels, capable of measuring in a single batch in three different directions. Finally, the non-linearity of the cervical tissue was explored, and it was adjusted to a proposed NL model and compared with the models present in the literature.

Resumen

La microarquitectura estructural de los tejidos blandos está recibiendo atención entre la comunidad de ingenieros biomecánicos y está aumentando el interés en el diagnóstico clínico en un amplio espectro de especialidades. El nuevo concepto científico de ultrasonido de ondas torsionales permitirá la cuantificación in vivo y no invasiva de una nueva clase de biomarcadores. Estos biomarcadores, que son medidas directas de las propiedades mecánicas de los tejidos, están íntimamente relacionados con la microarquitectura estructural de los tejidos blandos y son ideales para aplicaciones de diagnóstico. Esta visión estará habilitada por la tecnología única aquí propuesta que genera y detecta ondas de torsión en el tejido. El gran avance que supone esta nueva generación de biomarcadores físico-mecánicos tendrá un impacto a largo plazo. La funcionalidad elástica de los tejidos está íntimamente ligada a una variedad de patologías. Su medición cuantitativa in vivo constituye un principio de diagnóstico disruptivamente nuevo propuesto recientemente. Mucho más allá de los trastornos del parto y del parto (prematuridad, fallos de inducción, placenta, etc.), tiene un enorme potencial de extenderse para diagnosticar una gama cada vez mayor de patologías de alta prevalencia, incluidos los tumores sólidos (p. trastornos de los tejidos (lesiones de ligamentos, trastornos del envejecimiento) y fibrosis hepática, por nombrar algunos. La cuantificación de la funcionalidad elástica del cuello uterino no es actualmente una herramienta de diagnóstico estándar, ya que actualmente no existen tecnologías de cuantificación de la elasticidad o aún se encuentran en fase de investigación inicial. Una de las aplicaciones de dispositivos de ondas torsionales potenciales es la reducción de la mortalidad infantil. Al cuantificar las propiedades biomecánicas del cuello uterino en mujeres en riesgo, se puede identifiar con una detección suficientemente temprana el parto pretermino para que se puedan implementar las intervenciones adecuadas para retrasar la fecha del parto. La cuantificación no invasiva in vivo de las propiedades biomecánicas del cuello uterino será en enfoque clinico de este proyecto. Esto se logrará combinando la terоría subyacente, los avances tecnológicos necesarios para una sonda de diagnóstico mediante ondas torsionales, de prueba de concepto y algoritmos inversos basados en modelos para reconstruir la microestructura del estroma cervical para predecir su evolución elástica, y, por tanto, predecir su capacidad estructural de dilatar. Finalmente, este proyecto amplía en campo de aplicación, al-

lanando el camino a cualquier situación relacionada con modificaciones de la mecánica del colágeno, como la señalización celular mecanobiológica, el control del crecimineto tumoral, los procesos inflamatorios y de cicatrización, etc. y abre un nuevo y amplio campo de investigación con aplicaciones impactantes.
El grupo de investigación al que pertenezco ha desarrollado la técnica de elastografía por ondas de torsión y ha patentado un sensor isotrópico que ha sido validado in vivo midiendo en diferentes condiciones (presión y ángulo de incidencia) en mujeres embarazadas y voluntarias no embarazadas. Al mismo tiempo, se realizó la validación frente a un reómetro con muestras de tejido ex vivo. Mi contribución al trabajo se centra en la validación del sensor frente al estándar de oro: la elastografía de ondas de corte utilizando un sistema ventajoso verasonics de 256 canales. La validación se concentró al principio empleando fantasmas que imitan el tejido, tejido animal; hígado y mama. Cuando se manejó la técnica SWE, me concentré en muestras ex vivo del cuello uterino humano debido a la dificultad de obtener estas muestras. Los biomarcadores viscoelásticos se determinaron a partir de tejido cervical ajustando cuatro modelos reológicos. Hasta donde sabemos, estos resultados son los únicos valores que se han presentado utilizando esta técnica. Un paso adicional fue explorar cómo se comporta el sensor midiendo tejidos con diferentes capas, epiteliales y conectivos. La primera capa es mucho más fina que la segunda. Por tanto, para comprobar el tipo de ondas que se propagan en elementos con forma de concha, se diseñó un nuevo sensor para medir córneas y tener forma cóncava. La técnica de elastografía de ondas de torsión pudo detectar cambios en los tejidos debido a patología / daño y fue igualmente validada contra pruebas de elastografía de ondas de corte y máquinas de tracción. Los resultados concuerdan bastante bien. Otra contribución es investigar la anisotropía de tejidos blandos mediante el diseño y programación de experimentos de validación de un sensor de ondas de torsión sectorizado con tres canales, capaz de medir en un solo lote en tres direcciones diferentes. Finalmente, se exploró la no linealidad del tejido cervical y se ajustó a un modelo NL propuesto y se comparó con los modelos presentes en la literatura.

Abbreviations

ABC	Absorbing boundary conditions
ABS	Acrylonitrile Butadiene Styrene
ARF	Acoustic radiation force
ARFI	Acoustic radiation force impulse
CCI	Cervical consistency index
DE	Dynamic elastography
ECM	Extracellular matrix
FDA	Food and Drug Administration
FDTD	Finite difference time domain
FEAP	Finite element analysis program
FEM	Finite element model
FFT	Fast Fourier transform
FOEC	Fourth order elastic constants
GAGs	Glycosaminoglycans
GUI	Graphical user interface
HA	Hyaluronic acid
IFEA	Inverse finite element analysis
IQ	In-phase and quadrature
IQR	Interquartile range
ISPPA	Spatial peak pulse average intensity
ISPTA	Spatial peak temporal average intensity
KV	Kelvin-Voigt
KVFD	Kelvin-Voigt fractional derivative
M	Maxwell
MDG	Millennium development goals
MI	Mechanical index
MTL	Multiple track location
PBS	Phosphate buffered saline
PGs	Proteoglycans
PIP	Probabilistic inverse problem
PLA	Polylactic acid
pSWE	Point shear wave elastography
PTV	Particle tracking velocimetry
ROI	Region of interest
SCJ	Squamocolumnar junction

SDGs	Sustainable development goals
SE	Strain elastography
SMC	Smooth muscle cells
SPTB	Spontaneous preterm birth
sPTD	Spontaneous preterm delivery
SSI	Supersonic Imagine
SSR	Sum of squares of the regression
SST	Total sum of squares
SWE	Shear wave elastography
SWEI	Shear wave elasticity imaging
SWS	Shear wave speed
TE	Transient elastography
TH	Thickness
TOEC	Third order elastic constants
TOF	Time of flight
TU-SWE	Transurethral shear wave elastography
TWE	Torsional wave elastography
USTB	Ultrasound toolbox
WHO	World health organization
Z	Zener
3DMMRE	3D multifrequency magnetic resonance elastography

List of symbols

Symbol	Description
E	Young's modulus
μ	Shear modulus or Lame's second constant
ρ	Tissue density
K	Bulk modulus of elasticity or stiffness coefficient
c_s	Shear wave speed
ν	Poisson ratio
σ	Stress
ε	Strain
F_r	Acoustic radiation force
α_t	Tissue absorption
I	Spatial peak temporal average intensity or inertia moment
c	Speed of sound in tissue
$\mathbf{u}$	Vector of displacements
$\mathbf{f}$	Body force vector
λ	Lame's first constant, principal stretch or wavelength
σ_{ij}	Stress tensor
ε_{ij}	Strain tensor
δ	Kronecker delta or stress-strain phase lag
p	Hydrostatic pressure
v	Volumetric strain
τ_{ij}	Deviatoric stress tensor
d_{ij}	Deviatoric strain tensor
η	Shear viscosity
η^v	Volumetric viscosity
W	Strain energy
A	Third order elastic constant of Landau
D	Fourth order elastic constant of Landau
$tr\varepsilon$	Deformation trace
I_1	First invariant of strain
I_2	Second invariant of strain
I_3	Third invariant of strain

S_{ij}	Second Piola Kirchoff stress tensor
F	Deformation gradient tensor of volume force density
J	Determinant of the deformation gradient tensor or misfit function between model and observations
Ψ	Strain energy function
c_1, c_2	Mooney-Rivlin constants
μ_r	Infinitesimal shear modulus
α_r	Stiffening parameter
Θ	Torsion rotation
t	Time
ω	Natural frequency
n	Number of piezoelectric elements
a, b	Plane dimensions of the piezoelectric ceramic
d	Distance from the center of rotation
l^{eff}	Effective length between piezoelectric ceramics
h	Height of the cylinder or the ring
r	Radius of the cylinder or the ring or Pearson's correlation coefficient
m	Thickness of the ring in the radial direction
w/w	% Weight per weight
$^\circ C$	Degrees Celsius
G^*	Complex shear modulus
G'	Storage modulus
G''	Viscous or loss modulus
α	Fractional derivative power
μ_1, μ_2	Zener elasticities
σ_0	Stress amplitude
γ_0	Strain amplitude
∇u	Gradient of the displacement field
r, θ, z	Components in cylindrical coordinates
$\dot{v}_\theta$	Derivative of the velocity
$\ddot{u}_\theta$	Second derivative of the displacement
Δt	Time step
$\Delta r, \Delta z$	Space step of discretization
α_c	Correction factor
c_r	Factor of efficiency
Z	Shear impedance or acoustic impedance
t_T	Total time of simulation
n_{ABC}	Number of absorbing boundary conditions elements
N	Total population or random points
$\mathcal{O}$	Observations

$o_i(t)$	Observations signal vectors
$\mathfrak{O}$	Space of observations
$o^m(t)$	Model signals
$\mathcal{M}$	Model parameters
$\mathfrak{H}$	Manifold
$f(x)$	Information density function
$P(...), p(...)$	Probability
f^o	Experimental observations of the system
f^m	Numerical observations of the system
$\mathcal{H}$	Hypotheses of the models
$k, k', k_1, k_2, k_3, k_4$	Normalization constants
$\tilde{m}_i$	Change of variable
$\mathcal{N}$	Gaussian distribution
C	Covariance matrix
$\Delta\phi$	Phase change
ES	Effect size
F_c	Center frequency
P_0	Maximal acoustic pressure
T	Transmission coefficient
Z_{air}, Z_{water}	Acoustic impedance of the air and water
R^2	Coefficient of determination
p	P-value
$\mathbf{T}$	Piezoelectric material's stress
$\mathbf{C}_E$	Piezoelectric stiffness matrix
$\mathbf{S}$	Piezoelectric material's strain
$\mathbf{e}$	Piezoelectric coupling coefficient matrix
$\mathbf{E}$	Electric field
$\mathbf{D}$	Charge-density displacement
$\varepsilon_{\mathbf{S}}$	Permitivity coefficient matrix
L_{AB}	Length of the piezoelectric element in z direction
$\bar{\mathbf{E}}_3$	Average value of the electric field
$\mathbf{d}$	Piezoelectric coefficients matrix

Contents

List of Figures

List of Tables

Part I

INTRODUCTION

"I am one of those who think like Nobel, that humanity will draw more good than evil from new discoveries."

Marie Curie

Chapter1

Introduction

1.1.Project rationales and goals

The research group to which I belong has developed the torsion wave elastography technique (TWE) and has patented an isotropic sensor that has been validated in vivo by measuring under different conditions (pressure and angle of incidence) in pregnant women and non-pregnant volunteers. At the same time, the validation was done against a rheometer with ex vivo tissue samples. My contribution to the work focuses on validating the sensor against the gold standard: shear wave elastography using a 256-channel verasonics vantage system. The validation was concentrated at the beginning employing tissue-mimicking phantoms, animal tissue; liver, and breast. When the SWE technique was managed, I focused on ex vivo samples of the human uterine cervix due to the difficulty of obtaining theses samples. Viscoelastic biomarkers were determined from cervical tissue by fitting four rheological models. As far as we know, these results are the first that are presented using this technique. an additional step was to explore how the sensor behaves by measuring tissues with different layers, epithelial and connective. The first layer is much thinner than the second. Therefore, to check the type of waves propagating in shell-like elements, a new sensor was designed to measure corneas and have a concave shape. The torsion wave elastography technique could detect tissue changes due to pathology/damage and was equally validated against shear wave elastography and tensile machine tests. The results agree pretty well. Another contribution is to investigate soft tissue anisotropy by designing and programming validation experiments of a sectorized torsion wave sensor with three channels, capable of measuring in a single batch in three different directions. Finally, the non-linearity of the cervical tissue was explored, and it was adjusted to a proposed NL model and compared with the models present in the literature.

1.2.Impact

One of the most important potential torsional wave device applications will reduce infant mortality and childhood morbidity. By quantifying biomechanical properties of the cervix in at-risk women, sufficiently early detection of preterm birth may be identified so that suitable interventions can be implemented to delay birth. The noninvasive in vivo quantification of the biomechanical properties of the cervix will be the clinical focus of this project. This will be accomplished by combining the underlying theory, the technological advances necessary for a proof-of-concept torsional wave diagnostic probe, and model-based inverse algorithms to reconstruct the cervical stroma microarchitecture to predict its elastic evolution, and hence predict its structural ability to dilate. Finally, and most importantly, this project broadens the scope of applications, paving the way to any situation related to modifications of the collagen mechanics, like mechanobiological cell signalling, controlling tumour growth, inflammatory and healing processes, etc., and opening a new and broad field of research with impacting applications.

1.3. Thesis outline

This work is divided into the following sections: introduction) I will give some basic concepts of the questions to be dealt with. a) The structure of the soft tissues employed in this work and the techniques used to quantify their properties will be discussed. b) the definition of torsion waves c) soft tissue viscosity d) the propagation of shear waves in shell-like tissue and the anisotropy of the soft tissue. Finally, I will address some data about the hyperelasticity of the cervical tissue. In the methodology section, I will define step by step, a) the design of the three torsion wave sensors that are presented, how the measurements are executed, how the mechanical biomarkers are reconstructed b) I also explain the programming sequence script done to measure the shear waves using the gold standard in elastography, this the data processing, and the procedure for determining the group velocities of the shear waves. c) Finally, the methodology to validate the results obtained against tensile tests. The subsequent sections include a classic distribution that shows the results, discussion, conclusions, and future work.

"I am among those who think that science has great beauty."

Marie Curie

Chapter2

Preliminary concepts: Biomechanics of soft tissue

The soft tissue is responsible for supporting and connecting the different structures of the body. It can be said that almost the whole human body is soft tissue if we exclude bones, teeth and nails, considering that they differ substantially in their flexibility and mechanical properties. Soft tissue modelling can be done on several scales, including microscopic and macroscopic. This work deals with the second. The tissue is fundamentally composed up of three parts, the epithelium, stroma and mesenchymal cells [4]. The role of the different parts of the soft tissue will be addressed in the tissues that are mainly dealt with in this thesis; the cervix and the cornea.

Soft tissue structure is considerably complex; modelling it is challenging and requires close collaboration between the clinical and engineering communities. In 2003 [5], Humphrey has summed it up, saying that it has a *nonlinear, inelastic, heterogeneous, anisotropic character that varies from point to point, from time to time and from individual to individual.*

Soft tissue shows a dynamic behaviour under the effects of an applied load, varying from linear to nonlinear. This is why different mechanical models have been developed to try to capture this behaviour. These models include elastic (linear), hyperelastic (nonlinear elasticity), viscoelastic (time-dependent), and poroelastic (biphasic) types. Additionally, soft tissue can be characterized depending on its homogeneity and isotropy.

In this chapter, some brushstrokes are given to introduce the theoretical concepts treated experimentally in this thesis. Additionally, biomechanical explanations concerning the structure of the organs that have been explored to validate the proposed torsional wave technique experimentally are included.

2.1.Human uterine cervix as a biomechanical structure

The possibility of getting specimens of cervical tissue is limited to scientific cases and at-risk only. Therefore there is no availability of considerable numbers of samples, which limits an adequate breakthrough in the characterization of the aetiology of the cervix. The mechanical response in tissues such as the cervix is governed by its collagen structure. Several biological and mechanical changes cause disorientation in this structure during the gestation period, going from cross-linked fibres to just connected fibrils. Linking the variations on a microscopic biological scale to a macroscopic mechanical scale to achieve a multiscale approach to the problem becomes a valuable tool. Currently, there is no available clinical tool to evaluate the cervical biomechanical state quantitatively. For this reason, the WHO (World Health Organization) calls for innovation and research.

2.1.1.The cervix during pregnancy

- **Anatomy and physiology of the cervix:** From the moment a woman gets pregnant, biological changes occur; it is well known that these changes came from the combination of the growing pressures exerted by the fetus and endocrine processes that involves remodelling of the cervical tissue. It begins with biochemical reactions that affect the morphology of the tissue to the point of changing mechanical properties. The cervix serves two different functions: First, to protect from invading organisms from the vagina and maintain the fetus inside the uterus until the time of labour, behaving like a sphincter-like structure[6]. Second, move from a stiff mechanical barrier to a compliant structure that can dilate [7], serving as a guide to leaving the mother.

  The cervix is the cylindrical-shaped fibrous organ located in the lower part of the uterus, around 3 cm in length and 2cm in diameter[8] see Figure2.1. It is covered with epithelium, which is a tissue with an eminently protective function against infections and mechanical aggression. The elliptical convex part protrudes into the vagina is the ectocervix covered by a pinkish stratified squamous epithelium known as the

  exocervix visible zone speculum inspection. It is a non-keratinizing epithelium, which means that it cannot self-hydrate and possess a porous texture. It is composed of 15-20 cell layers. The division between the stroma and the epithelium is a single basal layer of cells with dark nuclei. It is usually a straight section, and however, sometimes there are inclusions of the stroma (stromal papillae). These projections become vascularized, providing nutrients to the epithelium[9]

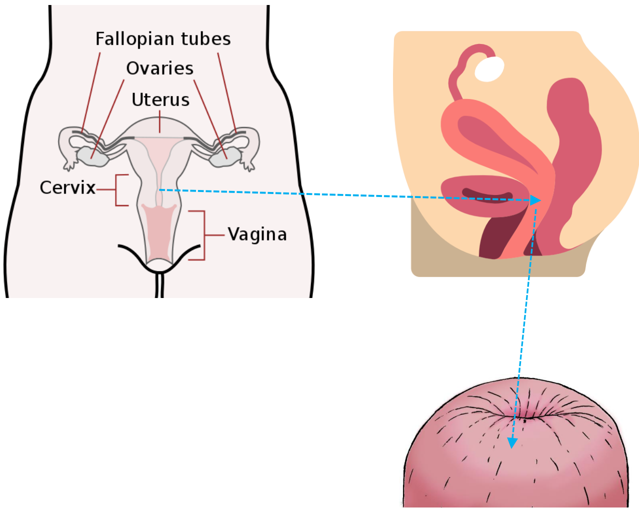

Figure 2.1: Human uterine cervix location

- **Phases of remodelling:** Pregnancy is a process of remodelling where the biochemical relationships within the stroma set up the new aspect of tissue. The duration of the procedure varies depending on the patient, taking into account her parity[10] and her BMI[11, 12, 13]. It is usually divided into four phases[14] which are superimposed as they occur until birth: softening, ripening, dilation and postpartum.

  1. **Softening:** Cervical softening is the first and most extended phase that commonly starts in the first month. It begins a slowly increasing turnover of ECM components, whose more visible result is the disorganization of the collagen network, which shows a decline in resistance, defined as compliance see Figure2.2. Nevertheless, the tensile strength(the integrity) is maintained. The compliance reflects the decrease in the elastic slope associated with unordered collagen fibres, elastic tension, increased water content and proteoglycans[15]. In the nonpregnant cervix, the epithelial cells are scant. However, during pregnancy, the hormone relaxin is implicated in their proliferation[16] when some prostaglandis(PGs) synthesis begins to be noticed. The cytokine interleukin-8(IL-8) appear[17].
  2. **Ripening:** Cervical ripening begins a few weeks before deliv-

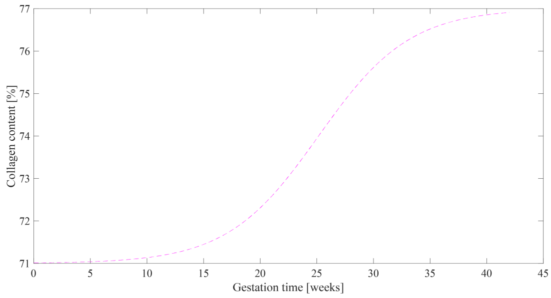

(a)

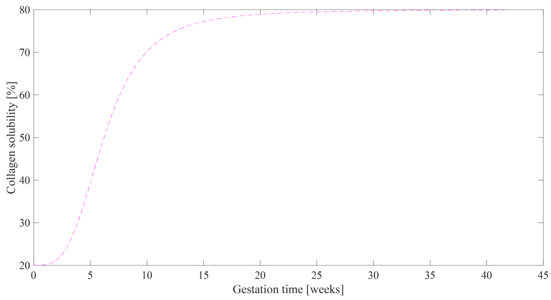

(b)

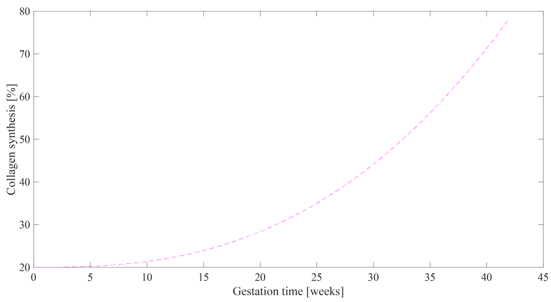

(c)

Figure 2.2: Collagen changes during pregnancy. a) Collagen content (b) Collagen solubility c) Collagen synthesis evolution . Adapted from [1] (CC BY 4.0.)

ery, and rapid changes in the cervix characterize it. It loses its integrity to prepare for the delivery. There is a marked increase in the synthesis of proteoglycans, collagen and hyaluronic acid (HA). Moreover, a hydrophilic glycosaminoglycan that interacts with epithelium cells and proteoglycans as versican. HA is in a considerable molecular weight to favour tissue hydration, resulting in a viscoelastic material, which unbalances the collagen network structure, dispersing and reducing its mechanical resistance[18, 19] due to increasing collagen solubility. Introducing progesterone inhibitors during softening has been proven to cause to reach maturation before[20], demonstrating that progesterone is a factor that maintains pregnancy. The loss of this hormone helps the estrogen to reach its receptors, facilitating the activation of ripening.

3. **Dilation:** The dilation of the cervix, preceded by biochemical changes caused by new hormonal regulation, contractions of the myometrium and the tension of the fetal protrusion, triggering the maximal loss of tensile strength. This process involves the infiltration of leukocytes, PGs, proteases and collagenases into the EMC[21, 22]. The protective mucus plug is expelled; in addition, it comes to a phase of effacement where the cervix narrows its walls and shortens to reach 10 cm in diameter. To complete the pregnancy, the female reproductive system must be transformed from a static formation to an active one with the coordination of its components. This coordination will lead to the final contractions that are transmitted through gap junctions. The continuous transition of the uterus to the cervix implies a reduction in the SMC content[23]. The circular and longitudinal architecture of SMC and collagen is maintained towards the cervix, ensuring a supporting force during pregnancy[24]. Myers et al.[25] identified a collagen remodelling with a four order magnitude reduction in stiffness. The contractions of the uterus are transmitted to the cervix, resulting in a progressive stretching towards dilation. At this point, the cervix resembles an elastic band, which begins to reach the elastic limit in dilation. Hence, the importance of the restorative phase in the postpartum.
4. **Postpartum:** The postpartum phase, the uterine involution, is meant to recover the tensile strength of the tissue, avoid environmental contamination, and prepare for ensuing pregnancies.

☐ **Cervix histology** The histological composition of the cervix began to be investigated in the 1960s on non-pregnant women, where two clearly differentiated zones were distinguished[26]:

- Smooth musculature 5-10%.
- Stroma 90%.

The musculature holds the functional part of the tissue, which is to prepare the cervix to dilate. Generally, studies have focused on the external os, which has more straightforward and direct access. However, Vink et al.[6]study measured that the content of smooth muscle cells (SMC) can reach 50-60% in the internal os, which a priori should not allow to extrapolate results to the whole set of the cervix. It should be remarked that this cell content is similar to that of the uterus, which along with gap junctions, a cell pathway for direct communication, can relate the remodelling of the uterus to the cervix. Stroma is the part of the tissue that ensures that musculature fulfils its mission by providing structural support. The cervix is considered a fibrous connective tissue since bundles of macromolecular fibres form its structure. These macromolecules are found within the stroma and are embedded in an extracellular matrix (ECM), where the most important biochemical reactions occur. The ECM composition can be differentiated into extracellular fluid with a content of approximate 75-80% and dry tissue of about 20% in content. In the latter, the main constituent is fibrillar collagen which forms a cross-linked network entwined with the protein elastin and enclosed by a ground substance of viscous proteoglycans and glycosaminoglycans that offers hydration and other matricellular proteins[27, 28]. A viscoelastic and heterogeneous point of view is required to understand the cervix[29, 30]. The study of Westervelt et al.[31]on the distension in the cervix employing finite elements, where geometric properties and materials were considered, deduced that the geometric parameters affected the most in the simulation softening. On the other hand, Fernandez et al.[32]proved that material properties must be carefully handled. The ECM provides strength and rigidity and has a crucial function during gestation, ensuring the integrity of the tissue.

2.1.2.Evaluation of cervical biomechanical properties

Although in the field of cervical tissue mechanical characterization, most of the works focus on dynamic methods, various techniques have been developed using different modalities, employing different tissue excitations and extracting different parameters of tissue motion. Some of these methodologies and their application in the care of cervical tissue can be found below.

Since the '70s, elastography has gradually become a widely applied medical imaging technique[33]. The principle of elastography is to induce a motion in the tissue so that a mechanical characterization is possible if the resulting displacements are followed. The difference in the mechanical excitations generated externally or internally led to the development of several elastography techniques. Therefore, different imaging modalities are used to estimate tissue displacement.

- **Quasi-static elastography/ strain imaging:** Quasi-static elastography or strain elastography (SE) was introduced in 1991 by Ophir et al.[34]. In the SE, static compression is used to deform the tissue. This stress can be induced by external palpation with the probe or endogenous stress such as cardiovascular movements to move the tissue. The displacements and the local strains are usually derived from the ultrasonic backscatter signals before and after compression by the 2D correlation of the ultrasound pre and post-compression data. The result is a qualitative deformation gradient map, called elastogram. SE is easy to implement but has limitations, such as the difficulty to compress deep organs. In addition, it is highly dependent on the pressure that the operator transmits to the tissue. Strain-induced by either cardiovascular pulsation or respiration can be used[35] to solve the limitation of SE of transmitting stress to deep organs. This has been used in deep organs like the liver[36]. The first elastography measurement in pregnant cervical tissue was performed by Thomas et al.[37]. In this study, they used static elastography to calculate the ratio of soft tissue to stiffer one during the pregnancy duration and tried to correlate it with the gestational age. After that, Thomas et al. [38]demonstrated no correlation of the tissue quotient with gestational age. Several authors used quasi-static methods to try to determine cervical stiffness during pregnancy. Molina et al.[39] used the hand to provoke tissue displacement to obtain cervical strain. For reproducibility, they also used quasi-static methods in 112 pregnant women in the four different zones of the cervix. Measurements were reliable except in the zone where the transducer exerts the pressure directly. Hernandez-Andrade et al.[40], in a posterior study, also suggested that there is a significant correlation between cervical strain and cervical length but much less correlation with gestational age. In their work, measuring was done in two different cervical regions. Several studies affirm that it is too soon to adopt quasi-static elastography to truly capture the changes that cervical tissue suffers during the gestational age considering that measurements are highly dependent on the pressure applied by the physician. Several works proposed the standardization of measurements[41, 42, 43]. The primary approach is to be able to control the loading applied on the cervix. Limiting the induced probe displacement was proposed by Molina et al. in[39], and controlling the compression by[40], others proposed using a reference elastomer material[44]. Fruscalzo et al.[45, 46, 47] used quasi-static methods to induce the tissue deformation. They aimed to measure the maximum deformability of the cervix. In summary, it seems there is no way to skip the limitation of strain elastography: the unknown applied pressure, quantification of absolute softness is impossible[48, 42, 49].

- ☐ **Dynamic elastography methods (DE)** Were developed to overcome the SE limitations and, mainly, to obtain quantitative elasticity maps. They are based on the propagation of shear waves within the tissue, which can be generated by a vibrating force in sonoelastography[50], a given frequency shift in vibroacoustography[51], in transient elastography[52] is a short impulsion or acoustic radiation force in ARFI and SWE[53].

  - **Acoustic radiation force imaging (ARFI):** Was introduced by Nightingale et al.[54]. This method uses focused ultrasound to generate localized displacement of a few microns via an ARF impulse within the tissue. In the time that lasts the impulse, the acoustic wave propagates through the tissue. Local displacements reflect relative mechanical properties of tissue and tissue deforms in response to the focused ARF excitation, so shear waves propagate away from it[55]. Finally, the displacement generated by the ARF is then mapped within the focal region of each push within a specified region of interest ROI at a known time after stopping the push. The tissue displacement response within the push region is directly related to the magnitude of the applied force and inversely related to the tissue stiffness[53, 54]. ARFI has been used in several clinical studies; examples can be found in[56] for breast, and in[57]for the prostate. The velocity of the shear wave generated by the ARF can be quantified in a small ROI and converted to elastic modulus[58, 59].
  - **Shear wave elastography (SWE)** Uses an ARF (Acoustic Radiation Force) to excite the medium and generate shear waves and produce a medium in a real-time quantitative elasticity map.

The technique can be subdivided into the creation of The Mach-cone, where ultrasound beams are focused successively at different depths to create spherical waves at each focal point. The different generated spherical waves interfere constructively along a Mach-cone creating two quasi-plane shear wavefronts propagating in opposite directions in the imaging plane[60]. Only one Mach-cone is needed to generate the quasi-plane shear wavefronts that travel across the medium to cover the entire ROI. The other division is Ultrafast Imaging, in which ultrasound plane waves are generated to track the shear wave displacement along the entire imaging plane with excellent temporal resolution in one single acquisition, typically up to 5000 frames per second. Therefore, there is no need to repeat the acquisition several times to acquire the entire displacement field. This allows imaging in real-time, which makes the examination easier[61].

– **Supersonic Shear Imaging (SSI)** Is an extension of the SWE method. It also quantifies the tissue elasticity estimating the shear modulus noninvasively and with a real-time image acquisition (30 milliseconds). SSI uses ARF pulses to generate shear waves and ultrafast ultrasound for tracking them[60]. The difference is that instead of simply transmitting one ARF pulse at a time, SSI transmits multiple ARF pulses in quick sequence, focal points differ marginally. The use of SSI possibilities the estimation of shear wave velocity (SWV) in a large area in one sequence. ARF pulses will generate shear waves that interfere with each other. Moving the focal point of ARF pulses is, in this case, a matter of moving a virtual shear wave source, and a source moving at supersonic speeds will create a Mach-cone. Because the source is moving faster than the shear waves, it is considered supersonic.

Non-evident results from SE to assess the cervical consistency motivated the use of dynamic elastography. Shear wave elasticity imaging (SWEI) is the most common form of dynamic elastography applied to the cervix[62, 63]. Shear wave velocity (SWV) can quantify tissue softness or stiffness because shear waves travel faster in stiffer and slower in softer tissues. Producing adequate shear waves in the cervix is not an easy job because we can not predict the wave generation in its boundaries. Even so, SWEI has been used to evaluate the pregnant cervix[64, 65, 11, 66, 67, 68]. In addition, the cervical tissue is highly attenuating because of its microstructural complexity.

Measurements of shear wave velocity were carried out by Carlson et al.[65] in human ex vivo hysterectomy samples. Their objective was to explore the feasibility of SWV to identify ripened cervices. Results show that SWV was capable of differentiating between ripened and unripened cervical tissue. H. Feltovich[41] suggested that elasticity is a very interesting biomarker for physicians since the elastic modulus varies more than 80kPa while SWV varies from approximately 1.2-5.5 m/s over the cervix. Ultrasound techniques have been used recently to expand our knowledge of the mechanical properties of the cervix. Carlson et al. [11] analyzed the feasibility of shear wave elastography, and they found that stiffness decreased with cervical ripening. Ultrasound waves over a wide frequency range were applied by Peralta et al.[69] the work shows that Maxwell's model is possibly the best rheological model for preliminary assessments of cervical viscoelastic properties. The work of Hernandez-Andrade et al.[70] manifested that it is unprovable to experience spontaneous preterm birth when pregnant women score small strain values at the internal os. Molina et al.[39] determined that the internal os and inferior portions of the cervix were stiffer than the external os and superior portions, same conclusions were obtained by Hernandez-Andrade[70]. SWV was evaluated in multiple areas of the cervix, and authors found that SWV decreased with increasing gestational age only at the internal os. Muller et al. found a decrease in SWV in women hospitalized for preterm compared to a control group[71]. Carlson et al. work about measuring the SWV before and after prostaglandin ripening before term induction of labour in 20 women determined a significant difference in SWV was reported (2.53$\pm$0.75 m/s before and 1.54$\pm$0.31 m/s 4 hours after prostaglandin application). A comparison of SWV between women in the first trimester and the third one was also made. Average SWV for 1st trimester was 4.42$\pm$0.32 m/s and 2.13$\pm$0.66 m/s for 3rd trimester[11]. Rosado-Mendez et al.[72]suggested that shear wave elastography can be improved, taking into account the viscosity of the region. In their study, they determined the viscous component of the cervix via the quantification of the shear wave dispersion. Tests were done in the Rhesus macaque cervix. Shear wave group velocity showed no difference between the prostaglandin-ripened and unripened cervix. However, taking into account local microstructure and viscosity seem to improve the accuracy of the cervical evaluation. Design numerical models for the pregnant uterus and cervix are very complex. In addition, it depends on the properties of the medium. Some numerical works were reported by Fernandez et al. SWV is determined assuming the tissue is homogenous and have an elastic behaviour[73]. However, the cervix is viscoelastic. Additionally, even small changes in collagen fiber waviness and diameter and orientation affect shear wave propagation velocity and dispersion[74].

2.2. Cornea

The mechanical status of the cornea is governed nearly entirely by the stroma [75]. The other layers that compose this tissue are considered to have secondary contributions, as in the endothelium, which functionality is cornea hidratation[76]. The mechanical stability of the cornea is due to the collagen, whose fibrils form stacked lamellae. This form of the fibrils makes a mechanism to resist shear and tensile forces[77, 78]. Keratoconus and other pathologies as post-surgery ectasia are caused by significant variations in the organization of the fibrils of the collagen layer[79, 80]. The increase in global elasticity[81] is because of the construction of new crosslinks within the stroma, in a related process to corneal crosslinking treatment (CXL)[82, 83]. The cornea's principal function, simultaneously with the lens, is to redirect light to the retina[84]. Contrary to the lens, the cornea has a fixed focus and cannot change its geometry to improve it. Consequently, the cornea's pathologies due to changes at the microstructure level affect its refractive capacity[85]. Evaluating mechanical biomarkers of the cornea, especially elasticity, could help in early diagnosis since it has been confirmed that alterations in cornea properties occur before any of the macroscopically visible structural changes in a clinical examination[86, 87]. Furthermore, the cornea is a viscoelastic tissue, and recent research works are trying to identify distinct viscoelastic biomarkers of the cornea[88, 89]. Encouraged by encouraging results in other soft tissues, several studies employed remote palpation by acoustic radiation force (ARF) to obtain 2D elasticity maps[90, 91, 92, 93, 94]. Polarized shear waves were induced within the field of view of the transducer, and then the displacements or velocities were tracked at a high frame rate as the waves propagated. These approaches provided valuable information, mainly due to their high resolution (>15 MHz), generating images with high sensitivity at the micro-level. Still, for the time being, it is challenging to re-engineer a clinical setup for its in vivo implementation, techniques that required transducer translation for imaging took tens of seconds, and the characterization of the applied acoustic force remains elusive, mainly due to the thin corneal geometry, where complex wave patterns governed by guided waves could bias the results[95]. Lastly, optical coherence elastography (OCE) stands as the most prolific technique in terms of publications[96, 97]. Studies used optical coherence tomography, where light-scattering measurements provided structural imaging, whereas OCE detected particle tissue displacements generated by mechanical loading to deduce viscoelastic parameters taking into account stress information. Its main advantages were the microscale resolution of the images and the microscale sensitivity in motion detection and the noncontact approach. Even so, it was not exempted from limitations, such as the low penetration depth, which was the trade-off for a micro-scale resolution (this was not a concern in the corneal application), long acquisition imaging times (>3 min), repeated stimulation that might lead to bias due to relaxation effects in the tissue and low frame rate in 2D imaging[98, 99].

2.3. Torsional waves

The clinical ultrasound community demands mechanisms to obtain the viscoelastic biomarkers of soft tissue in order to quantify the tissue condition and to be able to track its consistency. Torsional Wave Elastography (TWE) is an emerging technique proposed for interrogating soft tissue mechanical viscoelastic constants. Torsional waves are a particular configuration of shear waves, which propagate asymmetrically in-depth and are radially transmitted by a disc and received by a ring. This configuration is shown to be particularly efficient in minimizing spurious *p-waves* components and is sensitive to mechanical constants, especially in cylinder-shaped organs. The objective of this work was to validate (TWE) technique against Shear Wave Elasticity Imaging (SWEI) technique through the determination of shear wave velocity, shear moduli, and viscosity of ex vivo chicken liver, breast, tissue mimicking hydrogel phantoms, cornea and uterine human cervical samples.

Torsional waves are shear elastic waves that propagate through soft tissue radially and in-depth in a curved geometry. Application of torsional waves to sense soft tissue architecture has been proved to enable a new class of biomarkers that quantify the mechanical functionality of any soft tissue [100]. Abnormalities in the structural architecture of soft tissues are intimately linked to a broad range of pathologies including solid tumors, atherosclerosis, liver fibrosis, and osteoarticular syndromes [53]. The unexplored nature and applicability span of these mechanical biomarkers and torsional waves provides a very interesting diagnostic technology. The need for comparative and repetitive studies is clear. Validation studies are demanded due to the increased interest in the viscoelastic parameters obtained from elastography techniques [101].

In this study, the generation and detection of torsional waves through the proposed technology (TWE) developed by our group [102, 103] was used to obtain mechanical biomarkers in terms of shear wave velocity and shear moduli of ex vivo soft tissue.

Since TWE is an emerging technology, our objective was to compare scans of ex vivo liver samples with ones obtained from dynamic elastography techniques. Thus far, there is not enough scientific evidence in the literature to validate the most recent technologies. The first attempt to validate TWE was made by Callejas et al. [104] using classical rheometry. In this study, the validation was made using a Verasonics Vantage system (Verasonics, Inc., Kirkland, WA, USA). Shear waves were generated by an Acoustic Radiation Force Impulse (ARFI) to reduce some limitations of the previous work since classical rheometry works in a much lower frequency range than TWE. One important contribution of this work with respect to the prior is being able to compare the results of both techniques in the same frequency range.

2.4. Transverse wave propagation on bounded media

Previous studies have shown a close relationship between the optical system's visual function and the cornea's biomechanical properties [**?**]. Consequently, it is of immense interest to precisely determine these biomechanical biomarkers. For this, and when employing ultrasound elastography for tissue characterization, and due to corneas geometry (thickness of about 1mm) and position (enclosed by a softer and viscous fluid), the cornea is considered a plate-like tissue since the wavelength (λ 1-10cm) is way superior to its thickness [92, **?**, 91]. This consideration raises the concern that the relationship between wave velocity(c_s) and elasticity (E) does not follow the classical (pure) formula of $E = 3\rho c_s^2$ being ρ the tissue density. This formula is usually accepted in bulky organs since shear waves attenuate before reaching the organ boundaries. However, in plate-like tissues, shear waves propagating in the tissue experience multiple reflections on the boundaries, provoking guided waves. In the case of the cornea, and when the viscoelastic soft tissue is surrounded by fluid, the phase velocity $c(\omega)$ of a leaky Lamb wave can be determined from:

$$c(\omega) = \sqrt{\frac{\omega\, h\, c_s}{2\sqrt{3}}} \tag{2.4.1}$$

Where ω is the angular frequency, h is the plate-like tissue thickness and c_s is the group velocity given by shear modulus μ and density ρ by the equation $c_s = \sqrt{\mu/\rho}$. Equation 2.4.1 is a corrected formula of the classical Lamb wave for a plate in vacuum by a factor of $(1/\sqrt{2})$ due to the leakage of longitudinal waves at the wall interfaces [95].

2.5.Shear wave propagation in anisotropic media

Anysotropy is everywhere, to see, to measure and to model! Anysotropy is rare!

With the currently available technology, the characterization of the anisotropy of soft tissue is totally challenging. Determining the shear wave velocity in ultrasound elastography can only be done in one direction at a time. Therefore it is needed to make multiple measurements with different probe positions/angles. Furthermore, a simple model is often considered when estimating the anisotropic ratio, the transversely isotropic model, but only a few organs have this type of symmetry. To determine the full anisotropic tensor, we need technological development to access volumetric measurement of shear wave propagation[105]. The theory of elasticity studies the behaviour of solids with thermodynamically reversible deformations and independent of the deformation rate. If the outcome of the sum of actions is equal to the sum of the individual effects and the outcome of one action multiple of another is the exact multiple of the result of the mentioned action, the solid will be a linear system, and its behaviour will be studied using the linear elasticity theory. Even though most elastic solids have a non-linear behaviour, in reality, it is widespread to assimilate them to linear systems due to the regularity of their results and the predictability of their operation. Although the first expression of Hooke's law of evidence dates from the XVII century, the classical theory of linear elasticity was not developed until the XIX century, Cauchy, Navier, Poisson, Green or Saint-Venant. The constitutive equations of linear elasticity were established in the first half of the XIX century. However, they gave rise to a long discussion about the number of independent elastic constants necessary to define material behaviour (15 or 21 in the general case, 1 or 2 for isotropic materials). This controversy was not resolved until the beginning of the XX century when it was accepted that in the general case, the tensor contains 21 independent elastic constants [106].

The fundamental equations of linear elasticity in a rectangular Cartesian coordinate system $(x1, x2, x3)$ are the equilibrium equation

$$\sigma_{ij,j} - \rho\frac{\partial^2 u}{\partial t^2} + F_i = 0 \tag{2.5.1}$$

The constitutive equation

$$\sigma_{ij,j} = C_{ijkl}\varepsilon_{kl} \tag{2.5.2}$$

and the behavior equation

$$2\varepsilon_{kl} = u_{l,k} + u_{k,l} \tag{2.5.3}$$

where $\sigma_{ij} = \sigma_{ji}$ are the components of the symmetric stress tensor, $\varepsilon_{ij} = \varepsilon_{ji}$ are the components of the strain tensor, c_{ijkl} are the components of the fourth order tensor of elastic constants, u_i are the components of the displacement vector, F_i are the components of the force vector, ρ is the density of the material and t is time. The relationship established in 2.5.2 can be reversed

$$\varepsilon_{ij} = S_{ijkl}\sigma_{kl} \tag{2.5.4}$$

where S_{ijkl} is related to C_{ijkl} by the expression $S_{ijkl}C_{klrs} = \ delta_{ijrs}$.

The strain energy for anisotropic materials is

$$2\Phi = C_{ijkl}\varepsilon_{ij}\varepsilon_{kl} = S_{ijkl}\sigma_{ij}\sigma_{kl} \tag{2.5.5}$$

Substituting 2.5.2 and 2.5.3 in 2.5.1 the equation of equilibrium in displacements is obtained

$$E^*_{ijkl}u_{j,kl} - \rho\frac{\partial^2 u}{\partial t^2} + F_i = 0 \tag{2.5.6}$$

$$E^*_{ijkl} = (E_{iklj+E_{ilkj}})/2 \tag{2.5.7}$$

When solving particular problems, equations 2.5.1, 2.5.2, 2.5.3 and 2.5.6 are complemented with initial and boundary conditions. From 2.5.1 and 2.5.6 the equations of equilibrium are obtained under static conditions

$$\sigma ij + F_i = 0 \tag{2.5.8}$$

$$E^*_{ijkl}u_{j,kl} + F_i = 0 \tag{2.5.9}$$

Let n_i and m_i $(i = 1, 2, 3)$ be two unit orthogonal vectors. Young's modulus E_n at address n_i has the form

$$1/E_n = n_i n_j S_{ijkl} n_k n_l \tag{2.5.10}$$

The Poisson modulus nu_{mn} in the direction m_i for an applied stress in the direction n_i is

$$\nu_{mn}/E_n = -m_i m_j S_{ijkl} n_k n_l \tag{2.5.11}$$

The shear modulus G_{nm} between areas with n_i and m_i normal is

$$1/(4G_{nm}) = n_i m_j S_{ijkl} n_k m_l \tag{2.5.12}$$

The compressibility modulus K can be expressed as $1/K = S_{ijkl}$

Soft tissues can be modelled for study as transversely isotropic materials since they have a direction (the preferential orientation of the fibres) such that in planes perpendicular to it, their behaviour is isotropic. This class of materials only have five independent elastic constants. In this case, the constitutive equation can be expressed as

$$\begin{pmatrix} \sigma_{11} \\ \sigma_{22} \\ \sigma_{33} \\ \sigma_{44} \\ \sigma_{55} \\ \sigma_{66} \end{pmatrix} = \begin{pmatrix} C_{11} & C_{11} - 2C_{66} & C_{13} & & & \\ C_{11} - 2C_{66} & C_{11} & C_{13} & & & \\ C_{13} & C_{13} & C_{33} & & & \\ & & & C_{44} & & \\ & & & & C_{44} & \\ & & & & & C_{66} \end{pmatrix} \begin{pmatrix} \varepsilon_{11} \\ \varepsilon_{22} \\ \varepsilon_{33} \\ \varepsilon_{44} \\ \varepsilon_{55} \\ \varepsilon_{66} \end{pmatrix} \tag{2.5.13}$$

The elastic properties of the material and its density determine the speed of propagation of mechanical waves through it. We will focus on the case of shear waves as they are the most used for tissue characterization and those used in this work. The equation that relates the various parameters are obtained from the constitutive equation and the motion equation, assuming plane waves and taking into account the symmetries of transversely isotropic material. Thus, the speed of propagation of the wave is obtained from the expression

$$\rho c_s(\theta) = \frac{C_{44}C_{66}}{C_{44}sen^2(\theta) + C_{66}cos^2(\theta)} \tag{2.5.14}$$

where *theta* is the angle between the wave propagation direction and the fiber direction, c_s is the wave propagation speed, ρ is the density, C_{44} is the longitudinal shear modulus and C_{66} is the transverse shear modulus [**?**].

The values of the shear modulus G in the principal directions can be obtained using the simplified expressions

$$G(0) = C_{44} = \rho c_s^2(0) \tag{2.5.15}$$

$$G(90) = C_{66} = \rho c_s^2(90) \tag{2.5.16}$$

In order to obtain the G modulus, it is necessary to start from the wave velocity in the material. However, it is not measured directly but is calculated from the time t that the wave takes to travel a known distance d.

$$c_s = \frac{d}{t} \tag{2.5.17}$$

When measuring the time of flight of the signal, it must be considered fundamental to know the time needed by the wave to travel through the specimen material. Since, in general, the signal is not generated or received at the interface between the sensor and the sample, it is also necessary to take into account the time that the wave takes to travel through the measuring device itself. This time is called internal delay and is a specific value of each measuring device and must be rested from the measured value to obtain the calculated time.

2.6. Non linear shear elasticity

Modeling of soft tissue implies new perspectives that carry several clinical applications. It could be used, for example, in tissue engineering [107, 108, 109], for finite element modeling [110, 111, 112, 113], to analyze virtual reality in clinical practice [114, 115] and for surgery planning [116, 117]. To simulate those applications, the theory of linear elasticity has been employed to understand the results of mechanical tests on soft tissues [118, 119]. However, surgical procedures lead to consider large displacements and linear elasticity is a simplification when considering small strains. There is a need among researchers to use simplified models which can represent the nonlinear behavior of soft tissues. The simplicity of the proposed model in conjunction with a good correlation with the experimental data can be presented as an accurate and simple model in computational solid mechanics field.

Although the nature of soft tissue behaviour is viscoelastic [120], a simplification of hyperelasticity allows a reasonable characterization of the mechanical properties, specifically when the loss of strain energy is small (low loading rates). Veronda and Westmann [121] and Fung [122] were the first works that used hyperelasticity for soft tissue modeling. The hyperelastic approach postulates the existence of the strain energy function which relates the displacement of the tissue to the corresponding stress values [123]. The most common strain energy functions for the modeling of soft tissues are polynomial forms, such as Mooney–Rivlin and Ogden models. Many authors have modeled the behaviour of soft tissues such as, porcine spleen, porcine kidney, porcine liver, rat or human brain [124, 125, 126, 127, 128]. Regarding cervical tissue, uniaxial tension tests [129, 130, 131, 132, 133] and compression [131, 134, 135] have been studied in rat tissue and human tissue using load-relaxation protocols. A nonlinear stress–strain response has been shown in the tension and compression tests and the response of the tissue was noticeably stiffer in tension than in compression. It was observed that tissue from pregnant patients was one to two orders of magnitude more compliant than tissue from nonpregnant patients [131, 135]. In a work carried out by Yoshida et al. [133], load relaxation ring tests were performed on pregnant and nonpregnant rat cervices. The pregnant tissue showed a very large stress-relaxation compared to the nonpregnant tissue. Myers et al. observed that the cervix stiffness changes along its length in the uniaxial tensile test, where the external os had a stiffer response than the internal os [131]. The relationship between stiffness and gestational age was studied by Poellmann et al. and Jayyosi et al. [132, 136]. The works concluded that stiffness decreased as gestational age increased. In the works mentioned above were uniaxial, compression and traction tests were performed, the mechanical properties of the tissues have been obtained. However, in those works the nonlinear elastic properties of ex vivo human cervical tissue, using the Fourth Order Elastic Constants (FOECs), Ogden, and Mooney-Rivlin models have not been obtained through uniaxial tensile tests yet.

Soft tissues are composed of several layers; each one of these layers has different compositions, for instance, cervical tissues have an epithelial outer layer and a connective layer. The connective layer is composed by an extracellular matrix (ECM) that ensures the strength and integrity of the cervix, resisting shear deformation, through a fibrous scaffold [137]. The main component of the ECM is fibrillar collagen, which determines a cross-linked network interlaced with the elastin protein, enclosed by a ground substance of proteoglycans and glycosaminoglycans [138, 139, 140]. Researchers have identified three zones of structured collagen in the connective layer: the innermost and outermost rings of stroma contain collagen fibers preferentially aligned in the longitudinal direction, and the middle layer contains collagen fibers preferentially aligned in the circumferential direction [141, 142]. Regarding the collagen content, the middle zone had higher levels of collagen content when compared with the inner and the outer zones [142]. According to the mechanical studies on soft tissues, the connective layer is often considered as the most important from a mechanical point of view [143, 144, 145]. However, other studies, based on Torsional Wave Elastography, consider the epithelial layer as a key apart from the connective one [146, 104, 147]. The reason is that torsional waves not only propagate in depth but along the surface before being registered by the receiver. One of the purposes of this work is to study the differences in stiffness between the epithelial and connective layers of ex vivo human cervical tissue that comes from the hyperelastic models employed.

2.6.1. Theory of Hyperelastic Models

This section shows the theoretical relationship between stress and strain for a proposed hyperelastic model based on the FOEC in the sense of Landau's theory, Mooney–Rivlin and Ogden models.

Proposed Fourth Order Elastic Constants Nonlinear Model

Nonlinear FOECs are defined in the sense of Landau's theory [148] to establish a strain energy function, considering the medium incompressible valid for the hyperelastic regime as defined Hamilton and Destrade [149, 150],

$$\mathbf{W} = \mu I_2 + \frac{1}{3} A I_3 + D I_2^2 \tag{2.6.1}$$

where $I_1 = \mathrm{tr}\boldsymbol{E}$,$\mathrm{I}_2 = \boldsymbol{E}^2$ **and** $I_3 = \mathbf{tr}\boldsymbol{E}^3 \boldsymbol{E}^3 \boldsymbol{E}^3 \boldsymbol{E}^3$ are the classical invariant of deformation defined by Cemal

Figure 2.2: (**Left**): scheme of the uniaxial tensile test. (**Right**): zoom of a differential element of the sample. Adapted from [3] (CC BY 4.0.)

where the displacements are defined in three directions as,

$$\begin{aligned} u_1 &= ax_1 \\ u_2 &= -bx_2 \\ u_3 &= -bx_3 \end{aligned} \tag{2.6.2}$$

In this case, the Green–Cauchy strain tensor defined in Equation (2.6.1) may be described in matrix form as,

$$E = \begin{pmatrix} a + \dfrac{1}{2}a^2 & 0 & 0 \\ 0 & -b + \dfrac{1}{2}b^2 & 0 \\ 0 & 0 & -b + \dfrac{1}{2}b^2 \end{pmatrix} \tag{2.6.3}$$

To describe the Second Piola–Kirchoff stress tensor in a nonlinear regime, it is necessary to determine the invariant I_3 in terms of strains.

$$\begin{aligned} I_3 &= E_{11}^3 + E_{22}^3 + E_{33}^3 \\ \frac{\partial I_3}{\partial E} &= \begin{pmatrix} 3E_{11}^2 & 0 & 0 \\ 0 & 3E_{22}^2 & 0 \\ 0 & 0 & 3E_{33}^2 \end{pmatrix} \end{aligned} \tag{2.6.4}$$

The constitutive law for tensile test case in direction 1 is deduced by the expression,

$$S_{11} = 2\mu a + (\mu + A)a^2 + (A + 4D)a^3 \tag{2.6.5}$$

The relationship between the Cauchy stress tensor and the Second Piola–Kirchoff stress tensor is defined as,

$$\sigma = J^{-1} F S F^T \tag{2.6.6}$$

where F is the deformation gradient tensor and $J = det(F)$.

The derivation of Cauchy stress tensor in the context of weakly nonlinear elasticity [152] yields the constitutive law defined in high order as follows,

$$\sigma_{11} = 2\mu a+(5\mu+A)a^2+(7\mu+3A+4D)a^3+\left(\frac{5}{2}\mu + 3A + 8D\right) a^4+\frac{5}{2}(A+4D)a^5 \tag{2.6.7}$$

In order to compare with the other two hyperelastic models, the aforementioned tensor is simplified (using μ and A) as follows:

$$\sigma_{NL} = 2\mu a + (5\mu + A)a^2 \tag{2.6.8}$$

where a is defined in Equation (2.6.2).

Mooney-Rivlin Model

The Mooney–Rivlin model, originally derived by Mooney in 1940 [153] was formulated in terms of the Cauchy–Green deformation tensor invariants by Rivlin [154] as:

$$\Psi = \sum_{i=1}^{2} c_i \left(I_i - 3\right) \tag{2.6.9}$$

where c_1 and c_2 are the material parameters, I_1 and I_2 the first and second strain invariants respectively and Ψ the strain energy function.

In the case of an uniaxial tension ($\sigma = \sigma_1$, $\sigma_2 = \sigma_3 = 0$) the Cauchy stress as a function of the strain invariants is

$$\sigma = 2\left(\lambda^2 - \frac{1}{\lambda}\right)\left(\frac{\partial\Psi}{\partial I_1} + \frac{1}{\lambda}\frac{\partial\Psi}{\partial I_2}\right) \tag{2.6.10}$$

where $\lambda = \lambda_1$ (λ_1 is the principal stretch in 1 direction) and the invariants from the Cauchy–Green tensor for an incompressible hyperelastic material subjected to a uniaxial tension are defined as [155],

$$\begin{aligned} I_1 &= \lambda^2 + \frac{2}{\lambda} \\ I_2 &= 2\lambda + \frac{1}{\lambda^2} \\ I_3 &= 1 \end{aligned} \tag{2.6.11}$$

For the Mooney–Rivlin model, the Cauchy stress obtained employing (2.6.10) and using two parameters (c_1 and c_2) is,

$$\sigma_{\text{ Mooney}} = 2\left(\lambda^2 - \frac{1}{\lambda}\right)\left(c_1 + c_2\frac{1}{\lambda}\right) \tag{2.6.12}$$

Ogden Model

The strain energy function in the Ogden model, developed in 1972 [156], is described by,

$$\Psi = \sum_{r=1}^{N} \frac{\mu_r}{\alpha_r} \left(\lambda_1^{\alpha_r} + \lambda_2^{\alpha_r} + \lambda_3^{\alpha_r} - 3\right) \tag{2.6.13}$$

where μ_r (infinitesimal shear modulus) and α_r (stiffening parameter) are material constants, and λ_1, λ_2 and λ_3 are the principal stretches. Taking into account that for an incompressible material, $\lambda_1 = \lambda$ and $\lambda_2 = \lambda_3 = 1/\sqrt{\lambda}$ [155], Equation (2.6.13) is simplified into,

$$\Psi = \sum_{i=1}^{N} \frac{\mu_r}{\alpha_r} \left[\lambda^{\alpha_r} + 2\left(\frac{1}{\sqrt{\lambda}}\right)^{\alpha_r} - 3\right] \tag{2.6.14}$$

The Cauchy stress tensor as a function of the principal stretches for an incompressible material is,

$$\sigma_1 = \lambda_1 \frac{\partial \Psi}{\partial \lambda_1} - \lambda_3 \frac{\partial \Psi}{\partial \lambda_3} \tag{2.6.15}$$

Finally, using Equation (2.6.15), the Cauchy stress using two parameters (μ_r and α_r) is obtained as follows,

$$\sigma_{Ogden} = \mu_r \left(\lambda^{\alpha_r} - \lambda^{-\alpha_r/2}\right) \tag{2.6.16}$$

The shear modulus μ in the Ogden model results from the expression,

$$\mu = \frac{\mu_r \alpha_r}{2} \tag{2.6.17}$$

Part II

METHODOLOGY

"I am among those who think that science has great beauty. A scientist in his laboratory is not only a technician: he is also a child placed before natural phenomena which impress him like a fairy tale."

Marie Curie

Chapter3

Torsional Wave Elastography (TWE)

3.1.Sensor design and measurement configuration

The torsional wave sensor is based on a novel arrangement of concentric sandwiches of piezo- and electromechanical elements. The emitter transmitting the waves consists of a PLA (polylactic acid) disk, printed in 3D, whose rotational movement is due to an electromechanical actuator. The receiver is formed by two PLA rings with four slots in the inner face of the ring, where the four ceramic piezoelectric elements are fitted [157, 158, 146]. This allows the precise interrogation of soft tissue mechanical functionality in cylindrical geometries. Dealing with this type of geometry is a challenge for current elastography approaches in small organs.

Figure 3.1 shows the TWE probe developed by our group. The left sub-figure shows the sensor encapsulated in a CNC (computer numerical control) system that allows measuring within an exact position and at the same time exerting a controlled pressure on the sample. The right sub-figure shows a cross-section of the TWE probe. More details of the probe can be found in the work of Callejas et al. [104].

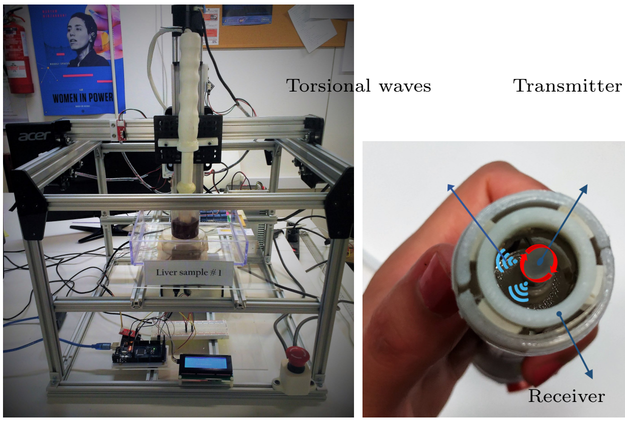

Figure 3.1: Set-up for measurements using TWE technique. The picture was taken during the measurements at the Ultrasonics Lab at the University of Granada. The figure on the left is a computer numerical control (CNC) system for positioning and pressure-control of the TWE probe. The right figure shows a cross-section of the TWE probe. Adapted from[2].

Time of Flight (TOF)- Signal Processing

Physically, torsional waves are originated by the actuator (transmitter, right part of Figure 3.1) and are transmitted through the specimens to the piezoelectric sensor, where they produce the deformation thereof and, consequently, an electric potential catchable by an oscilloscope.

To compensate for the mechanical and electronic crosstalk, a measurement is first taken in air, without contact with the specimen, which generates a signal transmitted mechanically inside the probe and electronically in air, under similar humidity conditions. This signal is stored and subtracted from the signals on the specimens, effectively compensating for the mechanical and electronic crosstalk. This signal is averaged 10 times for noise reduction, using a repetition rate that allows full dissipation of preceding waves. The total time of measurement is a quarter of a second, which is enough to register the desired frequency.

The remaining signal has traveled across the specimen and also through some mechanical parts of the probe. The apparent TOF is estimated from the subtracted signal as above, and after using a low pass filter at three times the center frequency, in three complementary ways: (1) by estimating the time where the signal amplitude surpasses 30% of the max level; (2)

by finding the first peak after that threshold; and (3) by finding the next negative peak, as indicated in Figure 3.2. The time of the theoretical signal start is estimated by subtracting the corresponding fractions of the period corresponding to the excitation frequency.

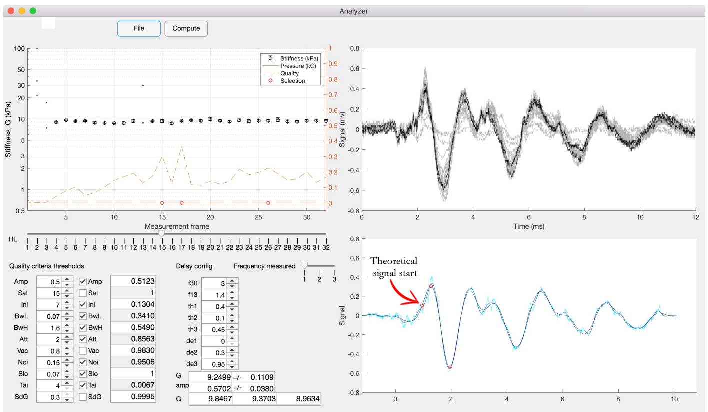

Figure 3.2: Example of an output of the analyzer software used to analyze the signals obtained from the TWE technique. The upper left sub-figure shows the stiffness obtained at each measurement frame. The lower-right sub-figure shows the theoretical signal start. Adapted from[2].

3.1.1.Isotropic TWE sensor: model for Human uterine cervix

The apparent time of flight (TOF) is, therefore, the sum of the TOF within the specimen plus the TOF across the components of the probe, which is called internal delay. The latter is a probe-specific constant that needs to be calibrated against SWEI and subtracted prior to computing the speed by dividing the distance by TOF within the specimen (Equation (3.1.1)), yielding Equation (3.1.2). Acquisition parameters for TWE technique used for both ex vivo liver samples and tissue-mimicking hydrogel are shown in Table 3.1.

$$c_s = \frac{\text{distance}}{\text{TOF}} \tag{3.1.1}$$

$$c_s = \frac{\text{distance}}{\text{TOF} - \text{delay}} \tag{3.1.2}$$

Table 3.1
Torsional wave elastography (TWE) technique acquisition parameters for both ex vivo liver samples and hydrogel phantoms.

Measurements Acquisition Parameters	**Value**
Sampling frequency	80 Hz (Decimated 10× after 800 Hz)
Ring-disc radius	3 mm
Frequency	200–800 Hz
Averaging	10 ×
Excitation power	20 V

3.1.2. Isotropic TWE sensor for Cornea samples

An elastography device with a matching design was proposed, where the excitation and sensor parts were assembled. The excitation generated torsional waves in the specimen by direct contact, which are in nature shear waves that propagate axisymmetrically, transmitting an oscillatory rotation through a cone-shaped disk (4 mm base) that was driven by an electromechanical actuator. Two parallel rings formed the sensor, with four slots in each inner face, where four ceramic piezoelectric elements (PZT-5) that worked on shear mode were connected with a conductive resin [32]. This configuration minimized the recording of unwanted compressional waves [35].

The dimensions and geometry of the contacting receiving ring were selected to match the samples [36], the external and internal diameters were 13 mm and 9.6 mm, respectively, with an internal curvature that covered the corneal shape completely. Under a sinusoidal excitation with different parameters such as frequency and amplitude, the actuator is subjected to a peak voltage during the measurement. Consequently, an interfering electromagnetic field is created; to avoid cross-talk, a Faraday cage was built around the actuator with aluminum foil to create an internal shielding effect. This set was assembled in a casing with mechanical attenuators that also centered the emitter disk relatively to the receiving ring (see Figure 2). All the components were 3D printed using a biocompatible photopolymer resin (MED610, Stratasys Inc., Eden Prairie, MN, USA) except for the casing that was printed in PLA (polylactic acid).

A multichannel AD/DA converter with 24 bits and 192 kHz sampling rate was used to generate and record the received signals. In principle, this sampling frequency increased the maximum wave speed limit sensitivity as compared to ultrasound elastography modalities. The digital to analogical converter output a single sinusoidal pulse of 600, 800 and 1000 Hz, the three frequencies used in this work, which was connected to a sound amplifier (100

W) that transmitted a load of 25V peak-to-peak to the emitter. Immediately after that, the recording step started and the receiver's electrical signal was captured by a preamplifier (40 dB gain), to finally reach the AD converter (see Figure 3). During this transition no interfering effect between steps was observed. A 5 kHz low-pass filter was applied to the received signal to eliminate the high-frequency jitter. In order to reduce random noise, the resulting signal consisted of an average of 10 signals, acquired at 200 ms time intervals, for a total measured time of 2 seconds. Prior to measure the sample, a calibration signal was taken to counterbalance crosstalk effects. A dedicated algorithm was used to calculate the group shear wave speed, where the theoretical start of the received signal was estimated and used as the time-of-flight (TOF) [37]. All the elements were computer-controlled using high-speed communications ports and a Matlab environment (The MathWorks Inc., Natick, MA, USA).

3.2. Anisotropic TWE sensor

3.3. Reconstruction of mechanical biomarkers

Acoustic radiation force imaging (ARFI) was introduced by Nightingale et al. [54]. This method uses focused ultrasound to generate localized displacement of a few microns via an ARF impulse within the tissue. During the impulse, the acoustic wave propagates through the tissue. Local displacements are related to the mechanical properties of the tissue, which deforms in response to the focused ARF excitation, thus shear waves propagate away from it [55]. Finally, the displacement generated by the ARF is then mapped, within the focal region of each push within a specified region of interest (ROI) at a known time after stopping the push. The tissue displacement response within the region of the push is directly related to the magnitude of the applied force and inversely related to the tissue stiffness [53, 54].

Shear wave elastography as ARFI also uses an ARF to excite the medium and generate shear waves and produces a quantitative elasticity map of the medium in real-time. The technique can be subdivided into the creation of the Mach-cone, where ultrasound beams are focused successively at different depths to create spherical waves at each focal point. The different generated spherical waves interfere constructively along a Mach-cone creating two quasi-plane shear wavefronts propagating in opposite directions in the imaging plane [159].

The Verasonics Vantage US research system is used to generate the push sequences and generate the shear waves. Verasonics is compatible with many transducers and offers big flexibility in sequence design. Additionally, Verasonics provides direct access to the raw channel data from each element of the array, as well as a software beamformer to form ultrasound images [160]. In Figure 3.3, one can see the Vantage Verasonics system during measurements and the Verasonics $L11-5v$ transducer used in this work is shown.

Figure 3.3: Set-up for measurements using SWEI. The picture was taken during the measurements at the Ultrasonics Lab at the University of Granada. In the left image, the ex vivo liver sample is measured while one of the hydrogel phantoms is shown in the right image. Adapted from[2].

The Verasonics vantage 128 system was used to perform the SWEI. The system uses the MATLAB programming environment to create the protocol of measurements of SWEI. The sequence of steps is as follows: the programmer writes a programming script to generate an imaging sequence, which generates a collection of objects that are loaded into the Verasonics scanner during runtime. The main parameters for the script are: (1) the push and track transmit frequencies; (2) the push duration; (3) the push and track transmit aperture; (4) the sampling frequencies; and (5) the pulse repetition interval. Details and sequences of the Verasonics script can be found in the work of Deng et al. [160]. In this study, a different transducer was used. Properties of the $L11-5v$ 128 elements linear array transducer are shown in Table 3.2.

Table 3.2
Properties of the $L11-5v$ Verasonics transducer.

Property	Value
Number of Elements	128
Pitch (mm)	0.3
Elevation focus (mm)	18
Sensitivity (dB)	-52 ± 3

Table 3.3 lists the SWEI acquisition parameters used in this study. The push transmit frequency was set to the center of the transducer to allow maximum transmission efficiency to transfer the ARFI to the tissue. An identical set can be used for the tracking frequency. However, it is recommended to use a lower push frequency to widen the push beam width compared with the track beam width to reduce the underestimation of tracked tissue displacement [161, 162] so a lower frequency was used.

Table 3.3
SWEI acquisition parameters for $L11-5v$ Verasonics transducer.

Parameter	Value for the $L11-5v$ Transducer
Push frequency (MHz)	4.8
Track frequency (MHz)	7.81
Push duration (cycles)	1000
Pulse repetition interval (μ)s	100
Impulse duration (cycles/(μ)s)	1000, 128
Impulse focus (mm)	16 for ex vivo liver and 12 for hydrogel phantoms
Beam focus configuration	Plane wave, fully open
IQ data beam forming sampling frequency	0.25λ
Excitation voltage (V)	40 for ex vivo liver and 28 for hydrogel phantoms
Sampling frequency(Hz)	3000
Number of transmission channels	128
Number of reception channels	128

Changes in the voltage applied for the push will make the induced push less or more powerful creating shear waves of different amplitudes. The voltage applied was stepwise increased and a value of 40 V was chosen for the ex vivo chicken liver and 28 V for the hydrogel phantoms.

3.3.1. Viscoelasticity and anisotropy of tissue mimicking phantoms

3.3.2. Viscoelasticity of ex vivo chicken liver and breast samples

3.3.3. Viscoelasticity and anisotropy and nonlinearity of ex vivo human uterine cervix

3.3.4. Viscoelasticity of ex vivo porcine cornea samples

Porcine corneal samples were obtained from a local slaughterhouse and enucleated immediately post-mortem, then placed in phosphate-buffered saline (PBS, pH 7.4) solution until testing. The buffer solution was prepared using di-Sodium Hydrogen Phosphate anhydrous (Reag. Ph. Eur. 99%), Potassium di-Hydrogen Phosphate (Reag. Ph. Eur. 99% purity) and Sodium Chloride (USP, BP, Ph. Eur. JP 99%) from Panreac AppliChem. To produce changes in mechanical properties, treatment solutions associated to alkali burns that modified the structure of the stroma were selected taking into account the most frequent chemical reactants that are contained in house or industry cleaning products [34]. A sodium hydroxide solution 1.5 M (NaOH) was used to simulate the most aggressive chemical exposure in the eye that can be caused by caustic soda. Sodium hydroxide salt was purchased from Panreac AppliChem (98%). Ammonium hydroxide 3 mM (NH4OH at 10% v/v) was used at a similar concentration as usual fertilizers and at double concentration found in cleaning products. Ammonium hydroxide solution (EMSURE® ACS, Reag. Ph Eur 28-30%) was purchased from Merck. Both treatment solutions were prepared in MilliQ water. All reactants were used as received without further purification. A total of 21 samples were tested within the first ten hours post-excision. They were classified considering the treatment and the exposure time, resulting in 5 groups (see Figure 1): control (N=5), NH4OH for 1 minute (N=4), NH4OH for 5 minutes (N=4), NaOH for 1 minute (N=4) and NaOH for 5 minutes (N=4). The treatment was applied to the entire eye globe by immersion in 50 mL of the respective treatment solution during the established time exposure. Then, the sample was washed in PBS and the epithelium was easily detached with the help of a spatula.

The whole porcine eyeball was placed in an immersed custom-built holder, and the cornea was orientated side up. The device covered the cornea with a gentle pressure, and all samples were measured three times by repositioning for averaging. Measurements were performed at atmospheric pressure. Preliminary safety considerations were examined. In this modality no cavitation-related problems were expected. Induced displacements were measured with an ultrafast ultrasound scanner (Vantage 128, Verasonics Inc., Redmond, WA, USA) that tracked the wave propagation with plane waves at a rate of 12.5 kHz, placing a 7.6 MHz transducer in a plane perpendicular to the emitter. Displacement peaked in control group at around 10 µm, thus, a linear regime was assumed. In a recent study with a similar configuration [33], the maximum acoustic intensity of TWE was estimated at 5.3 mW/cm2, well below the spatial peak temporal-average intensity limit of 17 mW/cm2 set by the FDA.

In the literature, there is a lack of corneal shear viscosity values for comparative purposes. In this work, and to shed some light on the viscoelastic biomarkers, elasticity, and viscosity, a simple Kelvin Voigt model has been used, which does the elasticity imaging community use as the most consensual model. Different works used a modified KV model with an additional spring (Kobayashi, glass) to separate the pure elastic and viscoelastic modes. On the other hand, Maxwell‘s model is not preferable to be employed since when a load is applied, it will continue to creep to infinity, and it also does not entirely reform due to its viscous component. Other studies have tried to associate corneal hysteresis with viscosity in air-puff applanation experiments.

3.4. Safety of torsional waves

In a recent study with a similar configuration [33], the maximum acoustic intensity of TWE was estimated at 5.3 mW/cm2, well below the spatial peak temporal-average intensity limit of 17 mW/cm2 set by the FDA.

3.5. Validation of TWE

3.5.1. Against SWEI

The measured shear wave velocity (SWV) can be used to determine tissue properties assuming a mechanical model of the tissue. For a linear, elastic, isotropic, homogeneous, and unbounded material, the SWV can be expressed in terms of the shear moduli μ and density ρ by the relation

$$SWV = \sqrt{\mu/\rho} \tag{3.5.1}$$

The density of soft tissue is typically assumed to be 1000 kg/m^3 and the SWV in units of m/s is equal to the square root of the shear moduli when it is expressed in units of kilopascals. In contrast, for a viscoelastic material, the shear moduli is a complex frequency-dependent quantity. Shear wave propagation in a viscoelastic material exhibits dispersion with a frequency-dependent phase velocity and shear attenuation [159].

The shear wave velocity dispersion curve was extracted from the ARFI using a phase difference method. First, the tissue velocity field was smoothed. This operation does not modify the phase velocity, only the amplitude, and the initial phase. The propagation of the plane wave in the sample along the x-direction is described by a 2D velocity field *v(x,t)*. The phase $\phi(x, \omega)$ of the wave at each frequency was obtained using a Fourier Transform of the tissue velocity field *v(x,t)*. For a monochromatic plane wave propagating in the direction x, the phase can be written as:

$$\phi(x, \omega) = -Re[k(\omega)]x \tag{3.5.2}$$

where $k(\omega)$ is the complex wavenumber and ω is the frequency. Thus, the shear wave phase velocity is:

$$c_s = \frac{\omega}{-Re[k(\omega)]} \tag{3.5.3}$$

and the real part $Re[k(\omega)]$ of the wave number can be estimated from a linear fit of the phase $\phi(x, \omega)$ along the propagation distance x [163, 164, 165].

Finally, dispersion curves are plots of shear wave velocity (SWV) as a function of angular frequency for ex vivo chicken liver samples and hydrogel phantoms.

Verasonics SWEI sequencing

Data processing: Tissue motion estimation

Tissue motion was determined using a phase-shift algorithm that operates on IQ data (in-phase and quadrature data). In this study, Loupas 2D auto-corrector algorithm was used to estimate the axial displacement caused by the propagation of the shear waves. The Loupas algorithm is an extension of the Kasai algorithm, which is used to post-process Verasonics data. It has the advantage of generating more accurate displacement estimations because it takes into account the center frequency [160, 166]. Figure 3.4 shows a flow chart of how Verasonics generates SWEI and the steps needed to obtain the IQ data from an ARFI sequence. In this work, post-processing of the IQ data to obtain a displacement map was done using the Ultrasound Toolbox (USTB) [167].

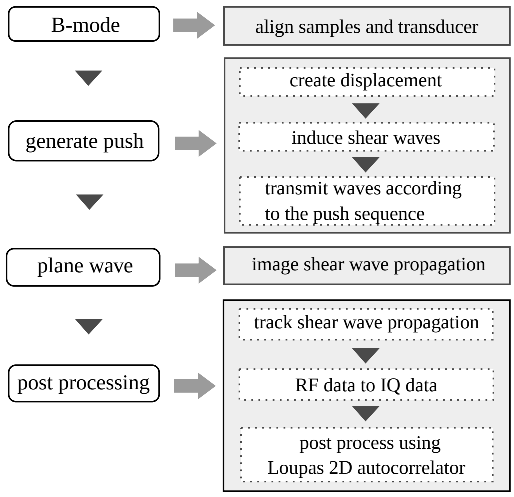

Figure 3.4: Procedure for tissue motion estimation using Shear Wave Elastography Imaging(SWEI) technique. Adapted from[2].

Group velocity estimation

3.5.2. Via mechanical tests

Uniaxial tensile tests were conducted to obtain the elasticity of porcine corneas in the five studied groups. The device used was designed and calibrated in the 'Ultrasonics Lab' of the University of Granada (Spain). It comprised two clamps, one that was firmly anchored to the base and another that could move in the vertical direction driven by three synchronized motors. The clamps were printed in ABS (acrylonitrile butadiene styrene) with specific surface roughness to avoid sample slippage. The upper clamp was attached to a digital force gauge (ZTS-50N, Imada Co., Ltd) whose maximum capacity was 50 N, with a resolution of 0.01 N. A high resolution camera with a 4:3 ratio and 2560x1920 resolution (IPEVO Ziggi-HD 5MPix) was synchronized with the displacement of the upper clamp. The monitoring of tissue deformation and the loading steps were controlled by a Matlab routine. All the samples were cut into vertical strips with the most unfavorable part being the central cross-section of the sample. The width of the NaOH-treated samples was reduced to avoid saturation of the force gauge. The dimensions of the samples were measured using an electronic caliper (Table 1). The samples were preconditioned with 10 loading cycles at 1 N to resemble a mechanical state close to in-vivo IOP conditions. The tissues underwent a quasi-static uniaxial tensile displacement to the rupture point at a rate of 0.2 mm/s. Acrylic black paint was sprayed over the sample for speckle generation in the samples to improve deformation monitoring. The corneal samples were kept continuously hydrated so as to prevent a severe alteration of the mechanical properties during the experiment by spraying them with PBS.

Although the stress-strain curve had a nonlinear behavior for the studied deformations, the curve was analyzed in two linear regions [39], where linear elasticity, homogeneity and isotropy were assumed, and viscosity ignored, which allowed to compare the trends with the values obtained with TWE. In the first region (toe region), the mechanical response was believed to be dominated by non-collagen components of the stroma, since the collagen fibrils were initially crimped and then were progressively uncoiling as the load increased. In the second region, collagen fibrils were sufficiently elongated to control the mechanical response (Figure 5). The stress-strain curve was obtained by dividing the force measured in each increment of displacement by the initial section in the most unfavorable area, and the deformation by dividing the displacement by the initial length between clamps. This initial length was set when the sample was stretched under a load of 0.01 N. The thickness of the samples was considered constant throughout the test. For the calculation of the elasticity in the first region, a linear range of deformation 0.02-0.04% was considered. For the calculation of the elasticity in the second region (mechanical response governed the collagen fibrils), a searching algorithm was implemented to detect the region of the curve in which the minimal variation of the slope was found between successive points.

Fig. 5. Tensile test setup and data analysis: a) front camera view, where a sample was clamped and attached to the force gauge at the top; b) typical stress-strain curve of a control group sample, the regions selected to estimate the elasticity modulus were a linear toe region K1 (non-collagenous response), and a linear collagen response region K2.

Hysterectomy Specimens

A total of seven hysterectomy specimens from women with benign gynecological conditions were obtained from Health Campus Hospital in Granada Table3.4). The study met the principles of the Declaration of Helsinki. Approvals of the Ethical Committee in Human Research of the University of Granada and Ethical Commission and Health Research of Health Campus Hospital in Granada were achieved. All women enrolled in the evaluation provided agreement by signing a written consent and reading the information of the patient report.

Table 3.4
Obstetric characteristics of the population in the study.

Patient	Age	Hysterectomy Indication
1	53	Vaginal prolapse
2	67	Subserous myoma
3	59	Vaginal prolapse
4	54	Cervical prolapse
5	50	Cervical prolapse
6	51	Cervical prolapse
7	71	Cervical prolapse

Mechanical Tests

All the mechanical tests were performed using the tensile-compression press shown in Figure 3.5. The device was equipped with a 500 N force gauge (IMADA ZTA-500N) fixed to a platform that is operated by three motors with an accuracy of 0.3μm. The tolerance of the force gauge is 0.1 N. The cervical tissue was fixed by two Acrylonitrile Butadiene Styrene (ABS) printed gripper jaws, one was attached to the press and another linked to a fixed support, that prevents the cervical tissue from undesired movements. According to the literature reviewed in soft tissue uniaxial tensile tests, the load step was 0.2 mm, and the strain ramp rate used was $1\%/s$ [168]. A rule was used in the same plane in which the sample was contained for the calculation of deformations. Finally, a conventional camera (IPEVO Ziggi-HD High Definition USB CDVU-04IP model, 5 Mpix, 1280 $\times$ 720 resolution) was employed to acquire the image sequence at each loading step until the sample breakdown (Figure3.6). The camera was synchronized with a MATLAB®programming environment (Release 2018b, MathWorks, Natick, MA , USA) at the beginning of the experimental test. The code implemented in MATLAB®allowed controlling each increment of load through an Arduino microcontroller, at the same time that recorded at a rate of 1 frame per load increment until the sample breakdown.

The sample preparation protocol consists of several steps:

1. All the seven cervical tissues were excised from the women and placed in phosphate buffered saline (PBS) to avoid loss of hydration after surgery. The connective layer was cut below the epithelial layer, and at a sufficient distance from the cervical canal to ensure that the pre-

ferred direction of the collagen fibers corresponds to the direction of the uniaxial tensile test [135, 169]. The samples were tested in the Ultrasonics Laboratory at the University of Granada. Two slices were cut manually from each cervical sample, one from the epithelial layer and another one from the connective layer. The epithelial layer was cut carefully to obtain a thickness between 0.5 and 1 mm. The connective layer was obtained below the epithelial layer. All the samples were cut with the same mold (see Figure 3.7) to maintain the same geometry, which is necessary to locate the most unfavorable section.

2. A random dot pattern was used in the cervix to improve deformation monitoring carried out by a cross-correlation algorithm (PTVlab software), see Figure 3.8. For the speckle generation, acrylic black paint was used.

3. An optimal contrast obtained by a good illumination and a uniform background help the tracking algorithm.

4. It is worth underlining that the cervical tissue samples were kept continuously hydrated so as not to alter the mechanical properties during the experiment by spraying them with PBS.

5. All the samples were preconditioned with 10 cycles at 1 N before the uniaxial tensile test.

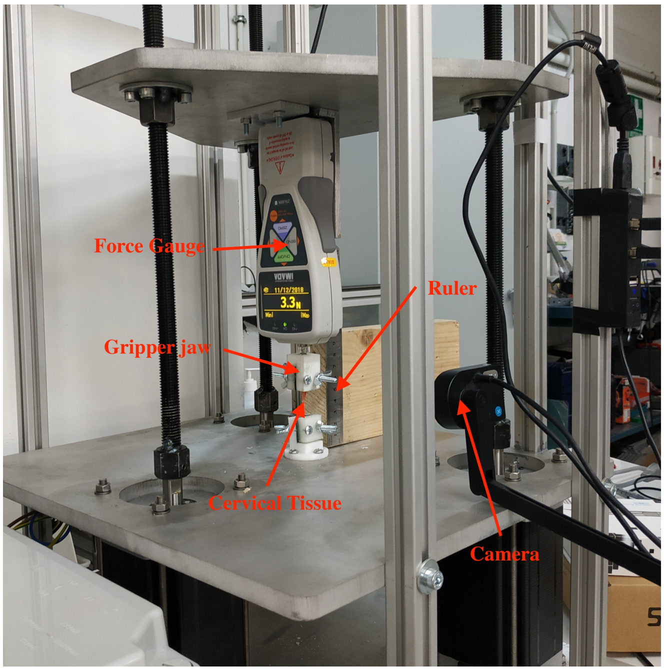

Figure 3.5: Experimental setup comprising a 500 N force gauge, gripper jaws for holding the sample attached and a conventional camera to register the loading process. Adapted from[3].

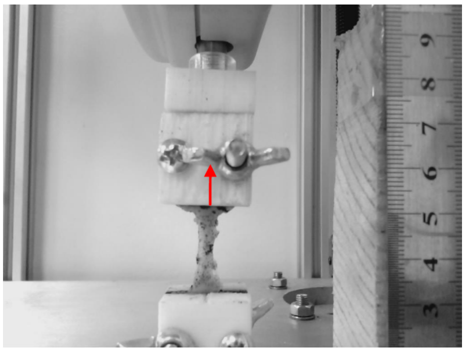

(a) Load = 2.8 N

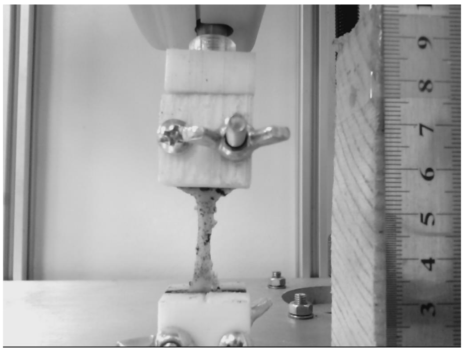

(b) Load = 10.7 N

(c) Load = 0.3 N

Figure 3.6: Three different frames from a recording of a uniaxial tensile test in a cervical tissue sample. The tissue is stretched in the direction marked with a red arrow. Adapted from[3].

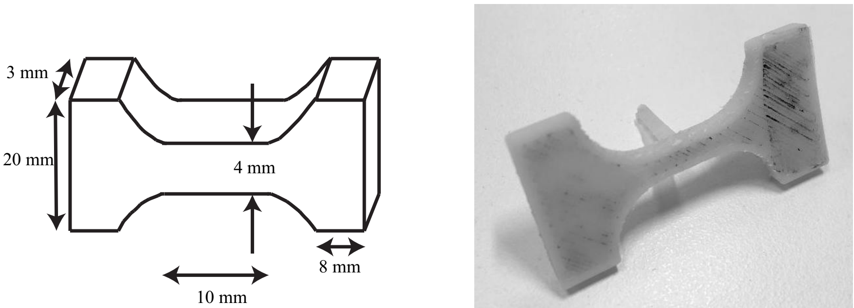

(a) (b)

Figure 3.7: (**a**) Mold printed with Acrylonitrile Butadiene Styrene (ABS) to maintain the geometry of the samples. (**b**) Cervical tissue sample geometry. Adapted from[3].

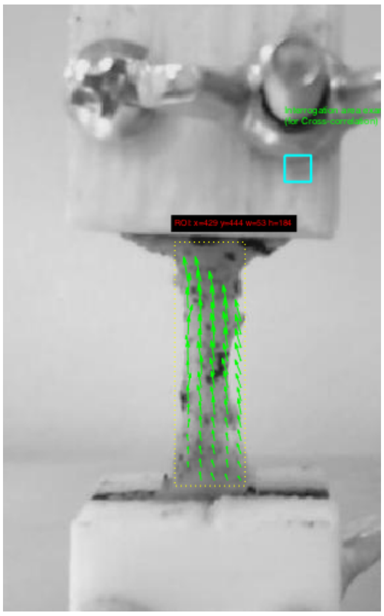

Figure 3.8: An illustrative example of cervical tissue attached to two gripper jaws that fix it during the uniaxial tensile test. A dashed yellow line was used to delimit the region of interest (ROI). The green arrows represent the displacements. Adapted from[3].

PTVlab is free software that was developed by Dr. Wernher Brevis (mainly developed the mathematical algorithms) and Antoine Patalano (an adaptation of the graphical user interface (GUI) in MATLAB and the development of new functionalities) [170, 171]. The Large Scale Particle Tracking Velocimetry (LSPTV) method is employed by PTVlab and uses the binary correlation, the Gaussian mask and the dynamic threshold binarization techniques for the particle detection. A Gaussian mask with a correlation threshold 0.5 and a sigma of 3 px was used for particle tracking. The Particle Tracking Velocimetry (PTV) algorithm was cross-correlated by an interrogation area of 10 px, a minimum correlation of 0.6 px, and a similarity neighbor of 25%. The deformations were calculated in the most unfavorable area of the cervical tissue, which according to the printed mold corresponds to the central area.

Part III

EXPERIMENTAL RESULTS

"Have no fear of perfection; you'll never reach it."

Marie Curie

Chapter4

Quantification of the mechanical biomarkers via TWE

4.1.Estimating tissue viscoelasticity of:

4.1.1.Ex vivo chicken liver

The results of the scans are presented as mechanical biomarkers in terms of shear wave velocity, shear moduli, and viscosity. A comparison of shear wave velocity as a function of frequency for both TWE and SWEI techniques can be found in Figure 4.1. The sub-figure on the top is for fresh ex vivo liver samples and the one on the bottom is for hydrogel phantoms. Measurements were done within the frequency range of 200–800 Hz. Solid lines are optimal fits of a Kelvin–Voigt rheological model.

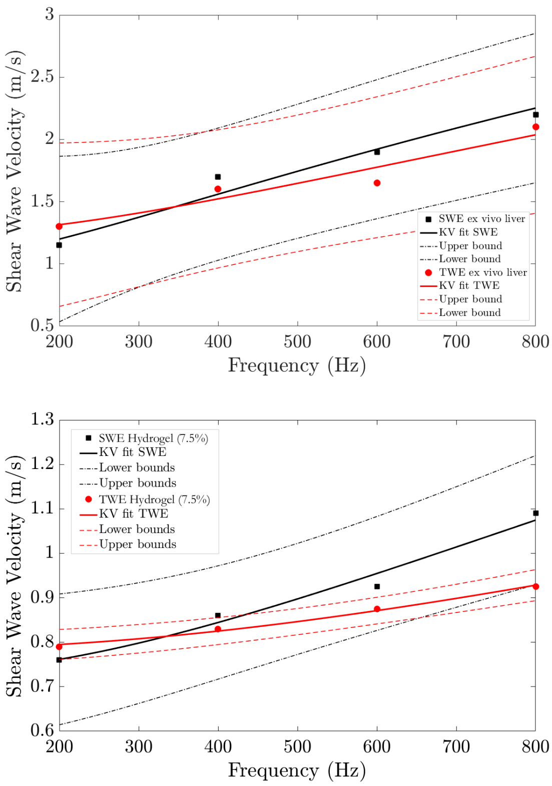

Figure 4.1: Dispersion curve for the two types of samples measured, square/circle marks are the values of shear wave velocity versus frequency via shear wave elastography imaging (SWEI) and torsional wave elastography (TWE) for ex vivo chicken liver samples (**top**) and hydrogel phantoms (**bottom**). Kelvin–Voigt (KV) fit is shown with solid lines in black color for SWEI and in red for TWE, and 95% confidence intervals are displayed with dashed lines. Adapted from[2].

The results show shear wave velocities go from 1.15 to 2.25 m/s for SWEI and from 1.3 to 2.03 m/s for TWE as mean values for the three liver samples. In the case of hydrogel phantoms, SWV values vary from 0.76 to 1.09 m/s for SWEI and from 0.79 to 0.93 m/s when scans were done via TWE. Both techniques show the same trend. These values are mean velocities for the two types of samples. ARFI based measurements were done three times in different liver areas. The results show a clear viscous trend in the samples. The results are in concordance with those presented in the literature [172, 173, 174].

A Pearson correlation coefficient was calculated to observe the degree of agreement between the reconstructed shear wave velocities obtained from both techniques, TWE and SWEI. The results are shown in Figure 4.2. A significant degree of agreement is observed, with a Pearson correlation coefficient of 0.99767 for liver samples and 0.99838 for hydrogel phantoms.

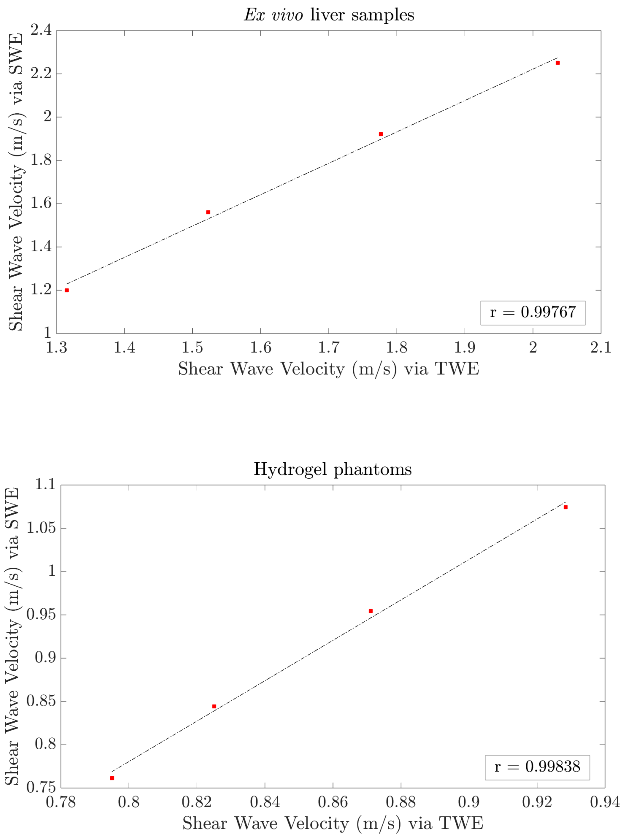

Figure 4.2: Pearson's correlation between shear wave velocities via SWEI and TWE for both ex vivo liver samples (**top**) and hydrogel phantoms (**bottom**) at a frequency range from 200 to 800 Hz. Pearson correlation coefficients are 0.99767 for liver samples and 0.99838 for hydrogel phantoms. Adapted from[2].

Biomechanical elastic parameters obtained via TWE and SWEI in terms of shear moduli, μ, for both ex vivo chicken liver samples and hydrogel phantoms are tabulated in Table 4.1. Scans were made under a range of frequency from 200 to 800 Hz. Measurements were done in this range of frequencies based on the power spectrum obtained from the shear wave tracked by the Verasonics transducer for liver samples, as shown in Figure 4.3. It can be observed that the energy concentration is within this range of frequencies (200–800 Hz); frequencies above this range are considered noise.

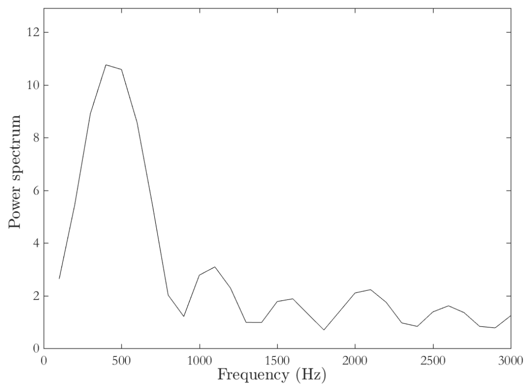

Figure 4.3: The power spectrum of the shear wave tracked by the 7.8 Mhz ($L11 - 5v$) transducer for the ex vivo liver sample using a Verasonics vantage system. Adapted from[2].

Next, viscosity parameters for the same samples using two different rheological adjustments, namely Kelvin–Voigt and Maxwell, were determined (see Table 4.2). The results show the same trend; shear moduli are frequency dependent and increases with increasing frequency.

Verasonics Vantage systems measure and report shear wave velocity; therefore, to obtain the mechanical biomarkers in kPa, SWV values were transformed by Equation (3.5.1) to get shear moduli μ. In this study, it was assumed that tissue density is 1000 kg/m^3.

Table 4.1
Shear moduli in kPa for both ex vivo liver samples and hydrogel phantoms obtained from torsional wave elastography (TWE) and shear wave elastography imaging (SWEI) techniques.

	Elastic Parameter: Shear Moduli in kPa			
	Ex Vivo Liver Samples		**Hydrogel Phantoms**	
Frequency (Hz)	μ_{TWE}	μ_{SWEI}	μ_{TWE}	μ_{SWEI}
200	1.69 ± 0.78	1.32	0.62 ± 0.04	0.58
400	2.66 ± 0.23	2.82	0.68 ± 0.05	0.74
600	2.69 ± 0.47	3.69	0.78 ± 0.065	0.85
800	4.00 ± 0.42	4.84	0.86 ± 0.055	1.16

Table 4.2
Viscoelastic parameters for ex vivo liver samples and hydrogel phantoms obtained from torsional wave elastography (TWE) and shear wave elastography imaging (SWEI) techniques.

Sample	**Fit**	**Viscous Parameters**				**The Goodness of Fit R-square**	
		TWE		**SWEI**		**TWE**	**SWEI**
Ex vivo liver	Kelvin–Voigt (KV)	$\mu = 1.512$ kPa	$\eta = 0.536$ Pa·s	$\mu = 1.019$ kPa	$\eta = 0.628$ Pa·s	0.9198	0.9572
	Maxwell (M)	$\mu_1 = 5.773$ kPa	$\mu_2 = 4.316$ Pa·s	$\mu_1 = 13.720$ kPa	$\mu_2 = 3.712$ Pa·s	0.835	0.9861
Hydrogel phantom	Kelvin–Voigt (KV)	$\mu = 0.615$ kPa	$\eta = 0.093$ Pa·s	$\mu = 0.532$ kPa	$\eta = 0.148$ Pa·s	0.9926	0.9764
	Maxwell (M)	$\mu_1 = 0.827$ kPa	$\mu_2 = 2.897$ Pa·s	$\mu_1 = 1.267$ kPa	$\mu_2 = 1.663$ Pa·s	0.7879	0.8237

Figure 4.4 shows particle displacement versus time profiles at 24 lateral positions for both an ex vivo liver sample and a hydrogel phantom.

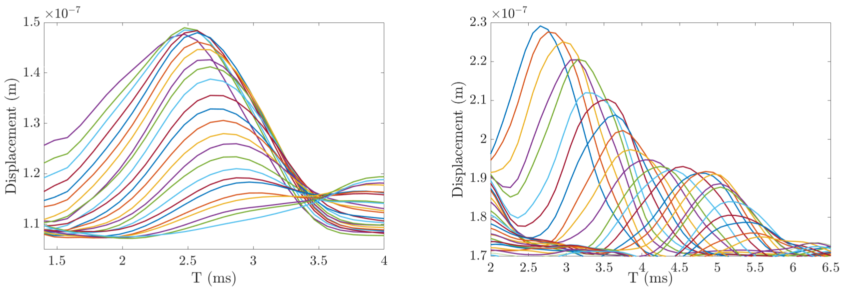

Figure 4.4: Experimental particle displacement versus time profiles at the focal depth resulting from the ARFI excitation. The ARFI moves the tissue in the axial and lateral position. In this figure, each displacement trace indicates a lateral position starting nearby the ARFI push focus to 24 lateral positions. Each individual color curve indicates the lateral position of a displacement trace for ex vivo liver sample II (**left**) and hydrogel phantom II (**right**). The curves show that, at farther distances (few milliseconds after the push), the particle displacement is reduced, since the shear wave dissipates. Adapted from[2].

The axial displacement map obtained using the Loupas algorithm [166, 167] after post-processing the IQ (in-phase and quadrature data) of ex vivo liver sample I is shown in Figure 4.5. We can see the ARFI push and the shear wave propagation. The y-axis represents the depth in mm of the scan, and the x-axis the lateral distance of the wave propagation. The sequence of the figure (from A to D) shows the localization of the ARF push and the shear wave lateral propagation away from the focus. Loupas $2D$ autocorrelator performs as the gold standard phase domain technique for motion estimation[175, 176].

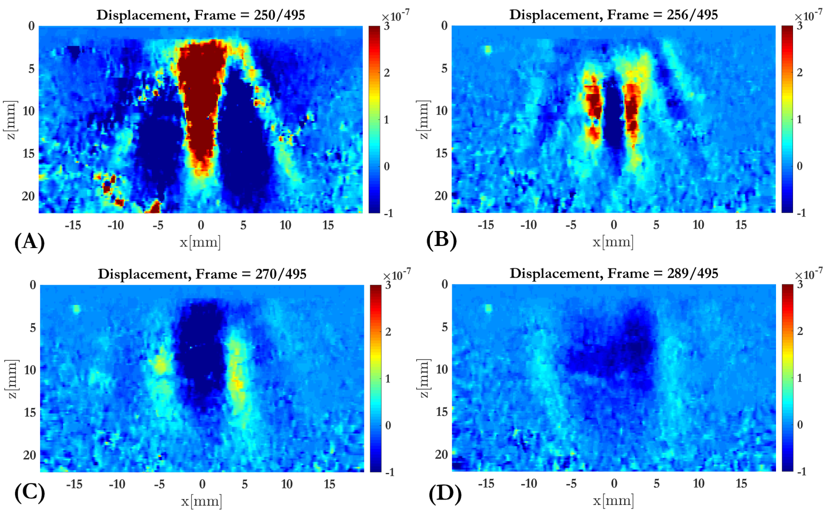

Figure 4.5: A sequence of displacement map (displacements are in meters) of ex vivo liver sample I due to ARFI excitation. The box represents the ROI (Region of Interest) chosen. The sequence from A to D show the push start (sub-figure A) and the shear wave propagation in different frames (sub-figures A-D) till its dissipation. Adapted from[2].

4.1.2.Ex vivo human uterine cervix

En este último capítulo se resume el trabajo desarrollado en la elaboración de esta Tesis y se enumeran las conclusiones más relevantes. Asimismo se destacan las tareas realizadas que han constituido aportaciones originales e innovadoras. Finalmente, se plantean posibles líneas de trabajo que podrían completar y ampliar algunos aspectos de interés relativos al estudio de propagación de ondas en problemas 2.5D.

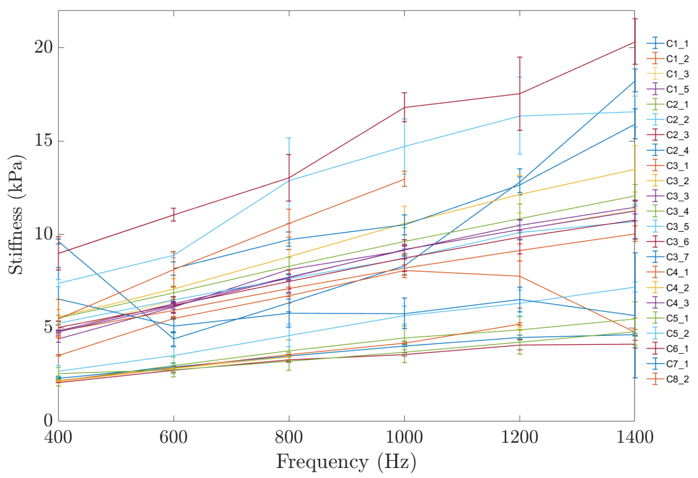

Figure 4.6: Stiffness values obtained from measuring via TWE the eight ex vivo human uterine cervix samples. Each sample was measured several times at different locations.

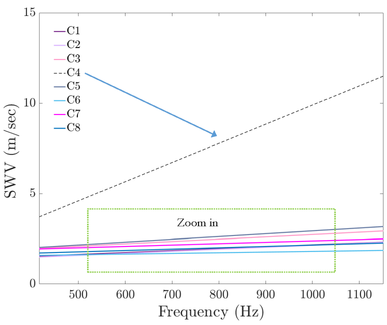

(a)

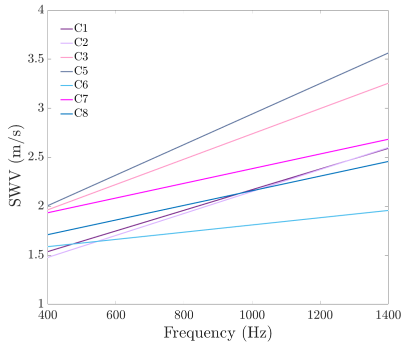

(b)

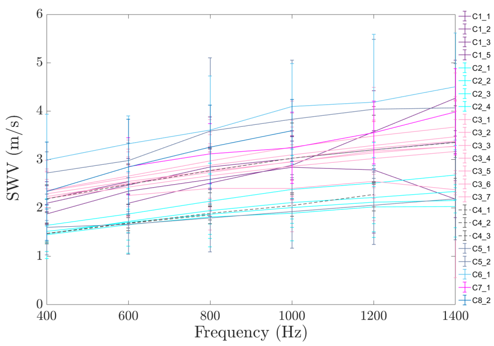

(c)

Figure 4.7: Group velocity values obtained from measuring the eight ex vivo human uterine cervix samples. Sub-figures a and b refer to Group velocity of shear waves using SWEI, while sub-figure c displays the same results via TWE. A) The total of the eight ex vivo samples is represented, so one can observe that the cervical sample number 4 shows anomaly velocity values (b) Is a zoom in from sub-figure a.

Table 4.3

Viscoelastic parameters obtained from fitting the TWE results in four rheological models; Kelvin Voigt, Maxwell, Zener and a Kelvin Voigt Fractional Derivate. Where μ is the elasticity in kPa, η is the viscosity in Pa.s, and α is the derivative power.

Cevix Uterine	**Kelvin-Voigt**			**Maxwell**			**Zener**				**Kelvin-Voigt Fractional Derivative**			
Sample	μ(kPa)	η(Pa.s)	R^2	μ(kPa)	η(Pa.s)	R^2	μ_1(kPa)	μ_2(kPa)	η(Pa.s)	R^2	μ(kPa)	η(Pa.s)	α	R^2
1	3.640	0.878	0.965	13.317	1.046	0.996	2.611	2.212	0.350	0.972	3.635	1.782	0.341	0.929
2	2.138	0.420	0.975	4.937	0.575	0.998	1.493	4.445	0.482	0.998	2.188	0.847	0.332	0.943
3	4.743	0.882	0.978	11.924	1.249	0.992	3.855	3.527	0.428	0.999	4.683	1.360	0.493	0.978
4	4.339	1.547	0.971	13.050	1.118	0.996	1.591	8.350	0.363	0.997	4.323	2.081	0.278	0.971
5	2.276	0.352	0.998	19.950	1.751	0.965	2.279	8.626	0.200	0.998	2.270	0.945	0.243	0.998
6	7.991	1.547	0.973	21.640	2.057	0.972	6.918	2.481	0.282	0.987	7.871	2.052	0.544	0.974
7	5.956	1.120	0.966	26.110	1.181	0.920	6.423	1.376	0.030	0.976	5.907	1.796	0.428	0.966
8	3.412	1.347	0.994	68.390	1.143	0.999	2.652	0.985	0.156	0.999	3.342	1.906	0.500	0.994

Table 4.4

Viscoelastic parameters obtained from fitting the SWEI results in four rheological models; Kelvin Voigt, Maxwell, Zener and a Kelvin Voigt Fractional Derivate. Where μ is the elasticity in kPa, η is the viscosity in Pa.s, and α is the derivative power.

Cevix Uterine	**Kelvin-Voigt**			**Maxwell**			**Zener**				**Kelvin-Voigt Fractional Derivative**			
Sample	μ(kPa)	η(Pa.s)	R^2	μ(kPa)	η(Pa.s)	R^2	μ_1(kPa)	μ_2(kPa)	η(Pa.s)	R^2	μ(kPa)	η(Pa.s)	α	R^2
1	2.250	0.386	0.991	17.110	0.453	0.984	1.753	5.083	0.295	0.999	2.193	0.441	0.691	0.990
2	1.533	0.480	0.999	41.080	0.404	0.989	1.576	3.862	0.239	0.999	1.526	1.967	0.157	0.999
3	3.000	0.775	0.999	14.870	0.814	0.983	2.938	3.000	0.246	0.999	2.241	0.802	0.878	0.979
4	10.71	9.150	0.7982	—	—	—	39.730	0.354	0.018	0.999	—	—	—	—
5	2.757	0.897	0.999	119.200	0.7386	0.990	2.998	1.815	0.127	0.999	2.744	4.461	0.129	0.999
6	2.545	0.262	0.989	2.318	0.979	0.928	25.560	3.165	0.276	0.999	2.450	0.898	0.188	0.989
7	3.465	0.5327	0.995	5.654	0.985	0.954	3.328	19.430	0.464	0.998	3.458	3.331	0.102	0.995
8	2.651	0.450	0.996	5.290	0.712	0.961	2.530	20.940	0.405	0.999	2.646	2.481	0.116	0.996

4.2. Viscoelasticity of ex vivo porcine cornea samples

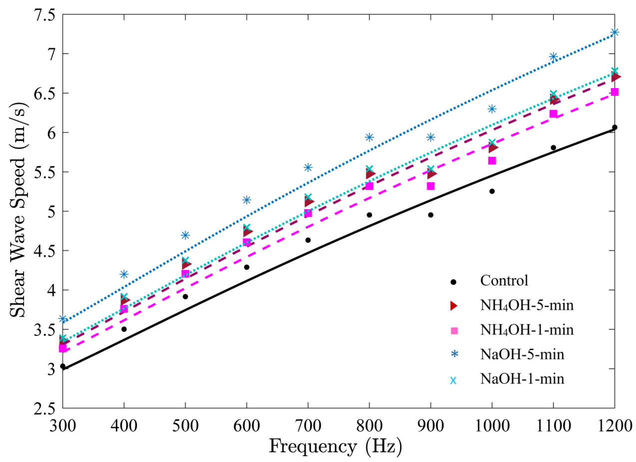

Figure 4.8: Experimental set-up for tissue characterization using Torsional Wave Elastography (TWE).

Table 4.5
Mechanical biomarkers: shear wave velocity and Young modulus as mean value of the five groups used in this study

	Shear wave velocity c_s (m/s)	Stiffness E (kPa)
Control	11.361±1.050	391.081±43.109
NH_4OH @5min	12.216±0.388	448.944±27.899
NH_4OH @1min	13.639±0.688	565.725±54.961
NaOH @5min	15.956±0.755	768.215±71.768
NaOH @1min	15.261±0.912	708.737±86.474

Table 4.6
Viscoelastic parameters for *ex vivo* porcine cornea samples using Kelvin Voigt (KV) fit for the Torsional wave elastography results

	Sample				
	Control	Amonia solution (NH_4OH)		Sodionm hydroxide (NAOH)	
Kelvin-Voigt fit		5min	1min	5min	1min
Elasticity μ(kPa)	5.112±0.413	5.573±0.637	5.611±1.151	6.611±0.628	6.080±1.002
Viscosity η(Pa.s)	2.835±0.228	3.091±0.353	3.112±0.638	3.666±0.3488	3.372±0.555

4.3. Assessment of shear stiffness using anisotropic TWE probe of:

4.3.1. Hydrogel phantoms

Table 4.7
Silicone phantom with aligned fibers measured by the different channels

Frequency (Hz)	silicone phantom with aligned fibers	Stiffness μ (kPa) 0° sensor	90° sensor	225° sensor
700	mean of 6 meassurements	179.549±6.306	84.342±3.445	123.771±3.886
1000	mean of 6 meassurements	207.560±6.193	90.452±4.585	144.424±4.126
1300	mean of 6 meassurements	229.926±3.977	106.715±4.958	177.075±5.856

Table 4.8

Tissue mimicking phantoms, without and with aligned and non-aligned 3D printed fibers measured with TW sensor

Control tissue mimicking phantom (without fibers)				
Frequency (Hz)	Mean Stiffness μ (kPa) and standard deviation			N=3
	0^o sensor	90^o sensor	225^o sensor	
1000	20.8827±2.6983	19.1632±3.2681	20.1189±2.5196	
Tissue mimicking phantom (with aligned fibers orientatet towards north direction)				
Frequency (Hz)	Mean Stiffness μ (kPa) and standard deviation			N=4
	0^o sensor	90^o sensor	225^o sensor	
1000	145.8259±34.4923	21.2633±1.0278	19.6110±3.2694	
Tissue mimicking phantom (with non-aligned fibers)				
Frequency (Hz)	Mean Stiffness μ (kPa)			N=5
	0^o sensor	90^o sensor	225^o sensor	
	37.7980	22.0811	26.7027	
	136.8140	8.2650	11.5826	
1000	39.6569	10.7216	9.7150	
	43.8111	37.7980	19.8619	
	106.1326	23.7739	15.8237	

Table 4.9
Ex vivo chicken breast measured by the different channels

Frequency (Hz)	Ex vivo chicken breast	Stiffness μ (kPa) 0° sensor	90° sensor	225° sensor
700	mean of 3 meassurements	40.752±1.407	16.247±1.631	32.258±0.960
1000	mean of 3 meassurements	43.573±1.555	17.848±1.073	33.603±2.017
1300	mean of 3 meassurements	56.253±2.359	19.846±1.644	36.719±1.198

Table 4.10
Ex vivo human uterine cervix measured by the different channels

Frequency	ex vivo human uterine cervix	Stiffness μ (kPa) 0° sensor	90° sensor	225° sensor
700	1	18.879±1.022	25.350±0.798	12.960±1.630
900	1	20.492±1.461	25.251±1.457	12.854±1.423
700	2	10.703±0.203	13.421±0.898	7.125±0.584
1000	2	20.534±1.511	26.997±1.578	13.413±1.207
900	3	32.863±2.738	56.020±3.805	22.230±2.909
1000	3	40.251±2.763	63.390±3.045	22.214±2.613

4.3.2. Ex vivo chicken breast samples

4.3.3. Ex vivo human uterine cervix

4.4. Nonlinearity of cervical tissue

4.4.1. Effect of applied pressure on the shear stiffness of ex vivo human uterine samples

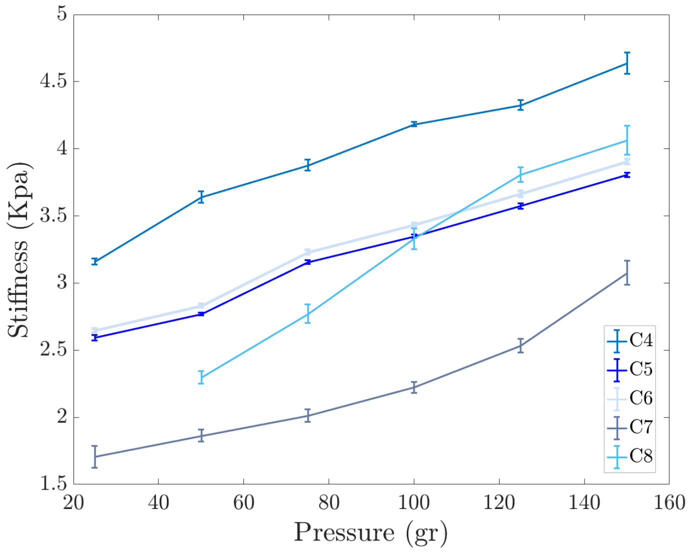

Figure 4.9: Effect of the applied pressure on the stiffness (a pressure ranging from 25 to 150gr was exerted). Measurements were done via TWE on ex vivo cervical samples.

4.4.2. Comparison between Hyperelastic Models

The experimental data of the uniaxial tensile tests for each of the cervical tissue samples are represented as stress–strain curves (Figure 4.10). In these curves, it can be appreciated the three zones that are explained in Figure 4.11: nonlinear, quasi-linear and rupture. The results of the fits of the experimental data with the three hyperelastic models are shown in Tables 4.11–4.13. These fitted curves were performed with MATLAB ® (Release 2018b, MathWorks, Natick, United States) Curve Fitting Toolbox. The median and the confident intervals have been calculated for each parameter. The relationship between woman's age and the Third Order Elastic Constant A from the proposed model, the infinitesimal shear modulus μ_r from the Ogden model, c_1 parameter from the Mooney–Rivlin model, and c_2 parameter from the Mooney–Rivlin model for the connective layer are shown in Figures 4.12–4.15.

An illustrative example of the comparison of the hyperelastic theoretical models with the experimental results obtained from the connective layer of Cervix 2 is showed in Figure 4.16.

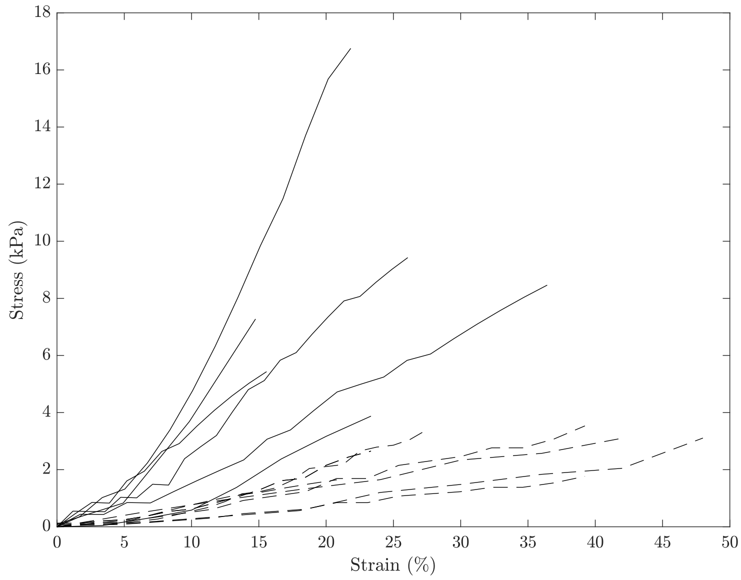

Figure 4.10: Experimental stress-strain relationship for cervical samples tested under uniaxial tensile test. Solid black and discontinue lines represent the connective and layer respectively. The stress is the true stress. Adapted from[3].

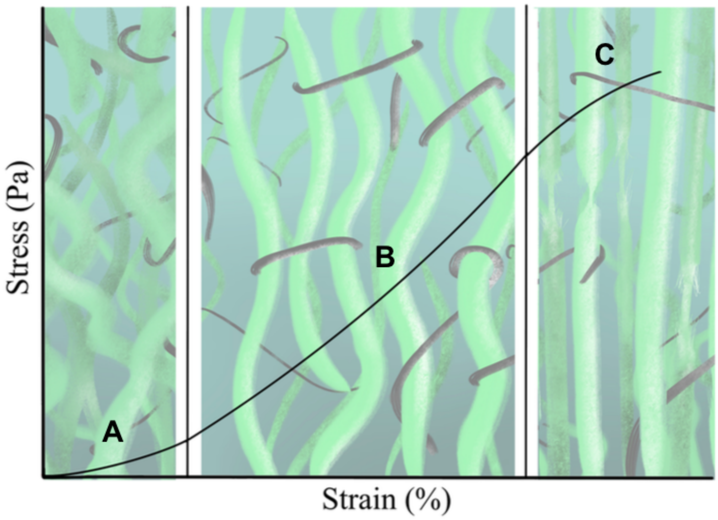

Figure 4.11: Representation of stress–strain behavior of soft tissues. The curve is divided into three zones: nonlinear (**A**), quasi-linear (**B**) and rupture (**C**). The state of elastin (black color) and collagen (green color) is represented at the bottom of each zone. Adapted from[3].

Table 4.11
Results of the fits of experimental data with the proposed nonlinear model. Shear modulus μ and TOEC A in MPa. IQR: Interquartile Range.

	Nonlinear Model			
	Epithelial Layer		**Connective Layer**	
Cervix	μ	A	μ	A
1	1.13	22.6	3.58	3.49
2	1.22	−6.08	4.72	−7.63
3	1.35	−3.06	2.64	−5.92
4	1.57	28.3	3.30	27.6
5	1.35	−2.35	3.51	73.6
6	1.13	2.32	3.49	70.1
7	1.27	30.72	3.96	25.7
Median (IQR)	1.27 (1.13 1.35)	2.32 (−3.06 28.3)	3.51 (3.30 3.96)	25 (−5.92 70.1)

Table 4.12
Results of the fits of the experimental data with the Ogden model. The infinitesimal shear modulus μ_r in MPa. IQR: Interquartile Range.

	Ogden Model			
	Epithelial Layer		**Connective Layer**	
Cervix	μ_r	α_r	μ_r	α_r
1	0.41	7.94	0.941	6.01
2	1.01	1.62	1.16	5.63
3	0.42	4.54	0.97	4.13
4	0.35	9.94	0.85	11.1
5	0.47	4.31	0.82	10.25
6	0.39	5.27	0.57	11.54
7	0.40	9.05	1.29	6.40
Median (IQR)	0.41 (0.39 0.47)	5.27 (4.31 9.05)	0.94 (0.82 1.16)	6.40 (5.63 11.1)

Table 4.13
Results of the fits of the experimental data with the Mooney–Rivlin model. IQR: Interquartile Range.

	Mooney-Rivlin Model			
	Epithelial Layer		**Connective Layer**	
Cervix	c_1	c_2	c_1	c_2
1	6.93	−6.73	5.87	−4.77
2	0.33	−0.08	4.7	−3.15
3	1.22	−0.78	2.51	−1.68
4	8.25	−7.84	59.9	−59.3
5	1.47	−1.05	20.56	−19.67
6	2.35	−2.06	15.7	−15.9
7	8.69	−8.44	12.1	−11.1
Median (IQR)	2.35 (1.22 8.25)	−2.06 (−7.84 −0.78)	12.10 (4.70 20.56)	−11.1 (−19.67 −3.15)

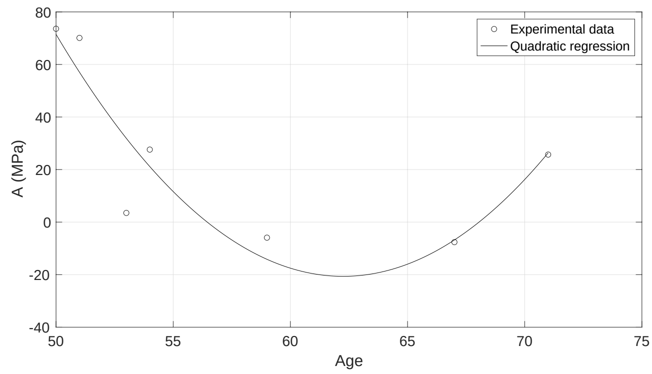

Figure 4.12: Quadratic regression of the Third Order parameter A of the connective layer against the woman's age. $R^2 = 0.84$. Adapted from[3].

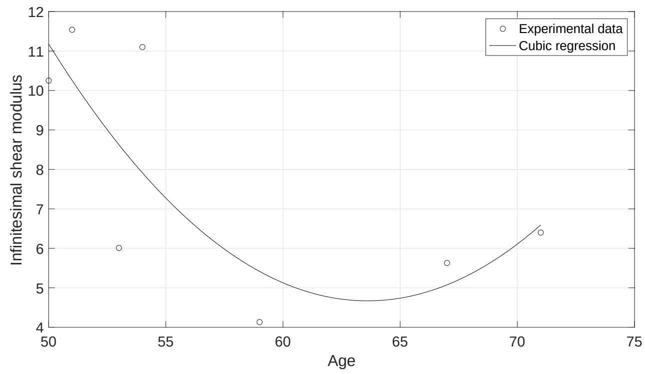

Figure 4.13: Cubic regression of the infinitesimal shear modulus μ_r of the connective layer from the Odgen model against the woman's age. $R^2 = 0.60$. Adapted from[3].

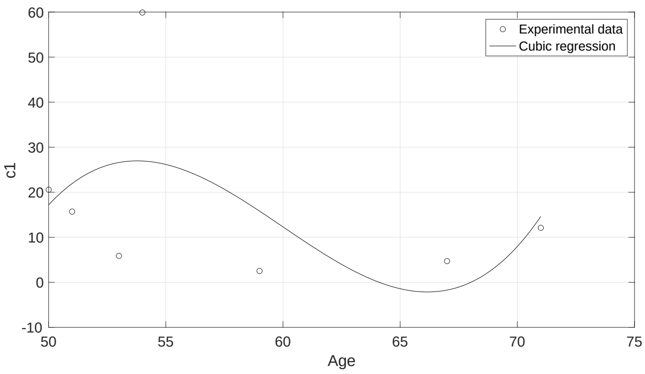

Figure 4.14: Cubic regression of the c_1 parameter of the connective layer from the Mooney–Rivlin model against the woman's age. $R^2 = 0.24$. Adapted from[3].

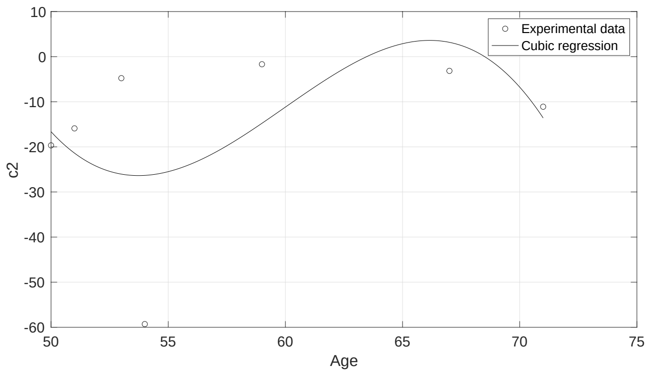

Figure 4.15: Cubic regression of the c_2 parameter of the connective layer from the Mooney–Rivlin model against the woman's age. $R^2 = 0.25$. Adapted from[3].

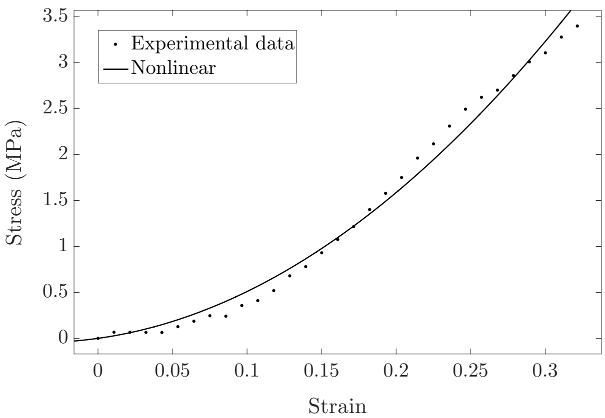

(a)

Figure 4.16: *Cont.*

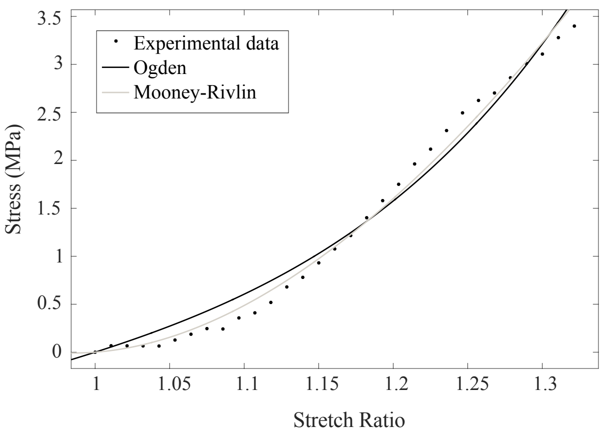

(b)

Figure 4.16: Comparison of the hyperelastic theoretical models with the experimental results obtained from the connective layer of Cervix 2. (**a**) The proposed nonlinear Fourth Order Elastic Constant (FOEC) nonlinear model; (**b**) Mooney–Rivlin and Ogden models. Adapted from[3].

4.4.3.Shear Modulus Estimation

The shear modulus can be obtained directly by means of the μ parameter of the FOEC proposed model, through the slope of the stress–strain curve in the linear region or also trough a combination of the two parameters of the Ogden model, the infinitesimal shear modulus μ_r and the stiffening parameter α_r (see Equation (2.6.17)). Table 4.14 shows the values of the shear modulus for each procedure and for each sample.

Table 4.14
Shear modulus estimation for the proposed nonlinear model, the Ogden model and the slope of the linear region of the stress–strain curve. The mean and standard deviation of the values for the seven samples are presented in MPa.

	Shear Modulus					
	Epithelial Layer			Connective Layer		
Cervix	**Nonlinear**	**Ogden**	**Curve**	**Nonlinear**	**Ogden**	**Curve**
1	1.13	1.65	0.82	3.58	2.83	4.17
2	1.22	0.82	0.69	4.72	3.28	3.78
3	1.35	0.95	1.43	2.64	2.01	3.62
4	1.57	1.77	1.82	3.30	4.71	3.26
5	1.35	1.02	0.44	3.51	4.22	5.25
6	1.13	1.03	0.90	3.49	3.30	4.42
7	1.27	1.84	1.08	3.96	4.15	3.17
Mean ± Std	1.29 ± 0.15	1.30 ± 0.43	1.02 ± 0.46	3.60 ± 0.63	3.50 ± 0.92	3.95 ± 0.72

In order to study the differences between the obtained shear modulus with the nonlinear model, Ogden model and the slope of the curve stress-strain for each cervical layer, a Student's t-test was used (see Figure 4.17).

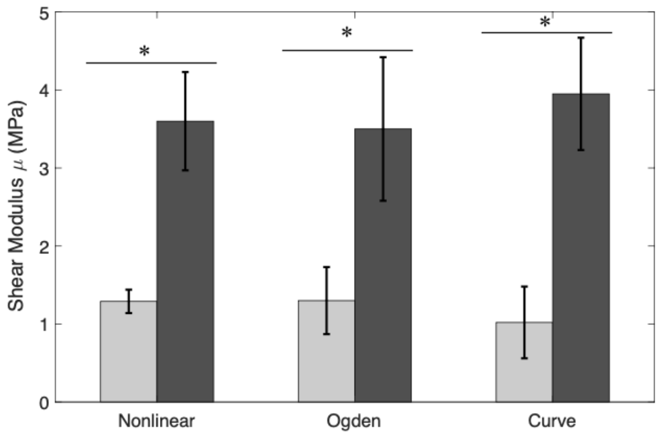

Figure 4.17: Comparison between shear modulus of epithelial and connective layers using the proposed nonlinear model, the Ogden model, and the slope of the linear region of the stress-strain curve. The results are presented as mean ± standard deviation. The light gray bars represent the epithelial layer and the dark gray bars the connective layer. P-value obtained from the Student's t-test was the metric used for this comparison. (* p-value < 0.001). Adapted from[3].

Another parameter that shows significant differences between the epithelial and the connective layers is the infinitesimal shear modulus. Figure 4.18 shows the mean and deviation values of the infinitesimal stiffness modulus, derived from the Ogden model, for the epithelial and connective layers. The metric used for the comparison was the p-value obtained from the Student's T-test.

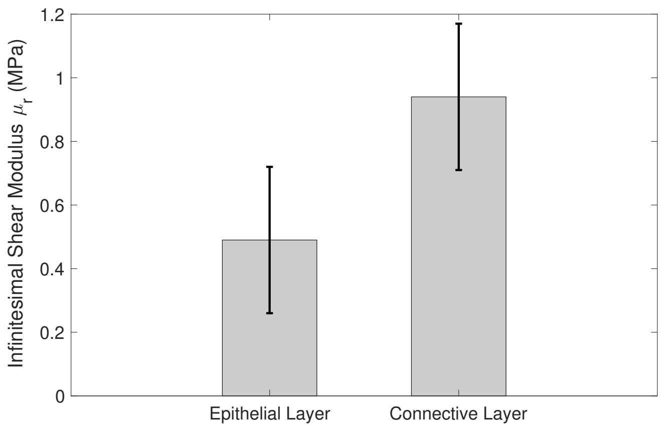

Figure 4.18: Comparison between the infinitesimal shear modulus (μ_r) of epithelial and connective layers using the Ogden model. The results are presented as mean $\pm$ standard deviation. P-value obtained from the Student's T-test was the metric used. (* p-value $= 0.0016$). Adapted from[3].

Part IV

CONCLUSIONS AND FUTURE WORKS

I was taught that the way of progress is neither swift nor easy.

Marie Curie

Chapter5

Discussion and conclusions

Objective 1: Tissue viscoelasticity

The principal goal of this work was to be able to reliably quantify the mechanical properties of soft tissue using Torsional Wave Elastography (TWE). A combination of information from different techniques is required in order to improve our understanding of the tissue mechanical behavior. Knowing cut off values of the different emerging technologies and comparing them with technologies well known and working as the gold standard in the field of the elastography would originate a strong impact on clinical diagnoses. It is an ambitious goal, yet we have obtained promising results and the technique is being validated through this work and recent work of the group. Torsional wave elastography has been shown to be effective in obtaining biomechanical biomarkers [104, 157, 158, 146, 145].

In this work, SWEI was used to validate TWE, since it is the gold standard and one of the most important noninvasive techniques in quantifying the viscoelastic parameters [177, 178]. A significant number of studies reinforce this decision; for instance, Kyoung et al. [179] showed that SWE is a good method to evaluate the usefulness of the stability index (SI) in liver stiffness measurements, demonstrating that this reduces the variability and increases the reliability in both free-breathing and breath-holding conditions. Samir et al. [180] estimated liver stiffness using SWE. The results obtained from the right upper lobe gave the best correlation with liver fibrosis severity and can potentially be used as a noninvasive test to differentiate intermediate degrees of liver fibrosis in patients with liver disease.

A validation study of five elastography techniques available commercially using individual tissue-mimicking liver fibrosis phantoms with different known Young's moduli was performed by Mulabecirovic et al. [181]. They concluded that the SWE systems have very good repeatability and interobserver agreement. Dietrich et al. [182] presented guidelines and recommendations on the clinical use of liver ultrasound elastography; in their work, they firmly recommend comparison studies of all the technologies available to improve our knowledge on cut-off values for each system. Another comparison among commercially available techniques using SWE for the assessment of chronic liver diseases was presented by Friedrich-Rust et al. [183].

The reproducibility of the TWE technique was evaluated and found consistent with previous studies. The first validation of TWE was made by Callejas et al. [104] using a classical rheometer (limited to 50 Hz), which is a quasi-static regime; the limitation of the previous work is that the measurements to obtain the shear moduli were made at frequencies well below the measurements made by TWE (300 Hz to 2 kHz). Therefore, in this work presented herein, the Verasonics Vantage system was used as the source to generate shear waves, allowing a comparison between the two methods in the same frequency range. The results are shown in Figure 4.1. The dispersion curves for the two types of samples measured, ex vivo liver samples and two tissue mimicking hydrogel phantoms, show the viscous response of the tissue. Each sample was measured several times by both techniques in different positions and under different pressures. Biological variability in the samples cannot be neglected; indeed, we observed different zones of rigidity in the same sample, which is true for all samples. Significant variability was found when different zones of the same sample were scanned by the same technique.

The values of shear wave velocities, from 1.15 to 2.25 m/s for SWEI and from 1.3 to 2.03 m/s for TWE as mean values for the three liver samples, agree with other results obtained from the literature [172, 173, 174]. However, the same figure shows that the curves representing TWE and SWEI results are spaced at high frequencies (>800 Hz). This is probably because the attenuation is too high and the signal is dissipated. A similar observation was obtained from the hydrogel phantoms results. Pearson correlation coefficient shows good agreement between shear wave velocity (SWV) via TWE and SWEI, with values of 0.99767 for liver samples and 0.99838 for hydrogel phantoms, as reported in Figure 4.2.

Elastic biomarkers in terms of shear moduli in kPa under the frequency range of 200 to 800 Hz show a good match between the techniques and report a similar tendency as SWV and therefore shear moduli are frequency dependent; increasing the frequency increases shear moduli values (Table 4.1).

One of the advantages of elasticity based images is that many soft tissues may share a similar capacity to reflect ultrasonic waves, but they may have different mechanical properties that can be used to visualize normal anatomy and trace pathological lesions more clearly. The liver is a viscoelastic structure, which is why changes in its viscosity would be closely related to liver diseases. Several authors suggest that changes in the transmission rate of mechanical vibration depend on the frequency [184, 185, 186]. Hence, SWE has some advantages over Transient Elastography (TE) [187, 188]. Since Shear wave velocity is frequency dependent, it is possible to quantify the tissue viscosity from the shear wave dispersion curves [189, 190, 191, 192]. In this study, viscoelastic biomarkers were obtained by fitting the model to the measured frequency. The results, as listed in Table 4.2, present significant differences between the two rheological models proposed, Kelvin–Voigt (KV) and Maxwell. The goodness of the adjustment shows that, in this case, KV model characterizes better both tissue samples and hydrogel phantoms. This opens up the debate to the elastography scientific community to present guidelines on which rheological model can express in the most concise way the characterization of soft tissue. Hydrogel phantoms show slightly better results than ex vivo liver samples, possibly for being more homogenous. Table 4.2 shows the parameters related to all the frequencies in the range of 200–800 Hz, where the maximum energy is concentrated, and not all the frequencies shown in Figure 4.3. Frequencies above 800 Hz are assumed to be noise.

TWE technique presents some advantages that make it interesting. First, it can reduce and isolate the spurious waves contamination (P-waves) [157, 146]. Another advantage is its ability to accurately interrogate soft tissue mechanical functionality in cylindrical geometries. Dealing with this type of geometry is a challenge for current elastography approaches in small organs such as the uterine cervix, where SWE would generate bounces on the tissue walls and mask the signal received by the receiver. However, TWE technique generates less energy that does not generate rebounds [158]. Torsional waves propagate both radially and in depth, which is very advantageous in the case of multilayer tissue. The technique is able to characterize the different layers of the tissue when there is a clear difference between the stiffness of both, since shear waves propagate more quickly in stiffer media. The path of torsional waves from the transmitter to the receiver depends on the tissue scanned; the methodology for the characterization of bilayer tissue mimicking phantoms using TWE can be found in the work of Callejas et al. [147].

Finally, TWE technique deposits extremely low energy in the tissue, which makes it exceptionally safe. When the acoustic waves are used for fetal imaging, three parameters should be evaluated for safety considerations. These mechanical and thermal index parameters and their values for TWE can be found in the work of Callejas [193]. TWE technique has already been successfully applied in vivo in a recent work by Massó et al. [145] to determine uterine cervix elasticity in pregnant women.

In this work, the tissue was assumed to be isotropic, but when highly anisotropic tissue is scanned the assumptions made are not precise. Taking into account the fiber orientation, the anisotropy of the soft tissue is still a pending subject of commercial elastographic techniques, including TWE.

Future directions should include a study of the attenuation versus distance, as well as exploring different soft tissues and more complicated rheological models for more robust and accurate estimations of viscosity. Additionally, in vivo scans should continue to validate the TWE technique in organs where it presents an advantage over SWE. In summary, this work demonstrates that the proposed TWE technique has enough potential in the determination of mechanical properties of soft tissues. Preliminary results of ongoing work in vivo are encouraging.
In this work, the authors present a Torsional Wave Elastography (TWE) technique developed by part of our group to determine the mechanical properties of soft tissue. The results were compared with the ones obtained from a commercial SWEI alternative. A programmable SWE-system for ex vivo samples was implemented and evaluated. The results of shear wave velocities and shear moduli for both ex vivo and hydrogel phantoms are in concordance with the literature. At the moment, we strongly believe that these results are promising and can be considered as a baseline for future studies on TWE. The objective was reached and TWE has been shown to be able to capture the tissue variability with respect to the frequency with a tendency close enough to the gold standard in elastography. Exploring the TWE technique in other soft tissues will be interesting future work, as will the study of attenuation versus time in in vivo measurements.

Objective 2: TWE in bounded media

In this study, the technical/practical capabilities of TWE were evaluated on a geometry as specific as that of the cornea. Unlike other organs such as the cervix [33] or liver [37], the translation to measure corneal elasticity was governed by the complex propagation of guided waves. A simple calculation of the group speed assuming pure elasticity might lead to significant bias [40], since generated waves are very dispersive, thus depending on the frequency range. In our case, the A0 mode was assumed to be the dominant mode at the response frequencies, for which an experimental expression had already been derived. Therefore, one small source of error was expected as the contribution of other guided wave modes was ignored, but possibly captured in the standard deviation of the estimation. Comparison between TWE and tensile test methods showed that calculated elasticities were coherent, registering higher values in the treatment groups with respect to the control group. The large difference between methods could be justified by experimental conditions inherent to destructive evaluation. The geometrical constraints imposed, such as clamping and the edges, and loss of curvature due to stretching, directly affected the microstructure. The tensile strain rate also played a role, due to viscoelasticity, since it was observed that higher rates resulted in higher elasticity [41]; yet it could be considered a convenient technique for comparative studies. In the literature, very mixed results were found, which are a consequence of the different time- and length-scales used, wave models, as well as experimental conditions, reaching ambiguous conclusions. Still, the elasticity values presented here were consistent with previous studies, ranging from 160 to 890 kPa under different setups and treatments [23], [24], [42], [43]. Experimental variations include IOP, a factor that was found to be positively correlated with elasticity [26], [44]. Increasing IOP stretches the cornea, introducing nonlinear elastic effects and affecting wave propagation [42]. However, very recently, Ramier et. al [43] found no correlation between these magnitudes, possibly due to a convenient distribution of stress in the human cornea in vivo. Another factor, essential during ex vivo experiments, is hydration. It is known to be a confounding factor due to corneal dehydration (no renovation of aqueous humor), resulting in tissue thinning and increased elasticity [2], [45]. Thus, thickness can be considered a surrogate of hydration in equation X, where higher elasticity was expected in thinner corneas. Interestingly, the difference in thickness between samples treated for one minute and the control was nearly significant, which may explain why 1 minute groups exhibited slightly higher shear elasticity. As the chemical treatment was more aggressive, a higher elasticity was recorded, for which it is hypothesized that instead of a weakening of the interlamellar integrity, at first, the alkali burn rearranged the components of the stroma through melting, whereupon the proteoglycan matrix would contribute by resisting higher deformation. Another possible explanation, was suggested by Nguyen et. al [46], where the removal of epithelium after treatment increased elasticity, probably due to dehydration and water regulation in ex vivo conditions.

The values presented by TWE were an average of global mechanical properties that translated into a fast reconstruction method, taking less than 7 seconds to calculate the group speed. In contrast to other techniques, where a map was reconstructed, no analysis artifacts were detected, such as diffraction or attenuation. However, some limitations of the current method need to be detailed. Only TOF algorithms are feasible to obtain the group speed, and then using expressions such as equation X, the significant dispersion and phase speed of waves are not considered. Boundary conditions like stress distribution generated by IOP confers a preload state, which could be modified if there is direct contact, biasing the results. It is likely that TWE missed focal abnormalities since no 2D image was obtained. The in vivo implementation of acoustic or optic-based techniques should improve the management of current applications, such as early detection of ectasia, corneal treatment customization, the role of IOP in pathologies such as glaucoma or the assessment of artificial corneas, just to name a few. Regular monitoring may indicate signs of corneal aging or degeneration, which should be taken into account for correcting measures such as tonometry. TWE has the potential to be integrated into conventional examination procedures, but there are a number of points that need to be further studied. Although there is direct contact, it is not a methodology unfamiliar with routine protocols such as tonometry, and therefore there is the possibility of using drops of topical anesthetic before contacting. Besides, a stable excitation is achieved in this modality, and by changing the diameter of the emitting disk, the exploitable frequency bandwidth of the response is expected to increase. To be on the side of safety, in the future the effect of the pressure exerted when measuring will be studied, both to assure an efficient propagation of torsional waves, confirming that local induced stresses do not severely affect wave propagation, and to avoid patient discomfort. On the other hand, this applied pressure could become an opportunity to obtain nonlinear elasticity parameters, as in acoustoelasticity, whose relevance could be substantial [34], [47]. Since it is difficult for patients to maintain a fixed position or avoid involuntary movements, the short times required to take measurements are an additional benefit that helps reduce motion artifacts. As recently reported [40], the use of Lamb wave models is required for a more accurate description of the viscoelasticity of the cornea, its feasibility with TWE should be studied. The measurement of corneal thickness here was done manually after removing it for tensile testing, but it can be done in vivo with pachymetry. Some studies suggested that the cornea is an anisotropic tissue with an accentuated mechanical heterogeneity, but when IOP was under 10 mmHg no dependency was found in the measured direction [23]. In the future, an anisotropic device will be developed to assess this aspect. In summary, corneal geometry, anisotropy, contact conditions and boundary conditions stand as relevant factors for a reliable mechanical quantification of the cornea.

This study used for the first time torsional waves as the source of excitation for elastography measurements in thin-layer corneal tissue. Corneas were subjected to chemical treatment to modify their mechanical behavior. An empirical expression was used to calculate the phase speed of A0 Lamb waves from the estimated group speed, through which the modulus of elasticity was obtained, and the dispersion curve was fitted to a Kelvin-Voigt rheological model. The trends of measured elasticity values were in agreement with tensile test results and literature reports, being TWE able to differentiate substantial changes, i.e., from 391.08 $\pm$ 66.03 kPa in control group, to 738.47 $\pm$ 132.21 kPa in NaOH-treated group. Shear elasticity was within the range of thin-layer tissues, whereas shear viscosity has not been reported after the used empirical Lamb wave expression. The management of corneal surgery and treatments should not solely depend on complex models of geometry and topographical parameters, but also rely on quantifiable mechanical parameters that improve diagnostic sensitivity, changing from generalized empirical-based models to customized approaches. Futures studies should implement a suitable Lamb wave model, and prove the feasibility of using TWE with in vivo animal studies in combination with standard equipment.

Objective 3: TWE for anisotropic media

The preliminary results are promising; the transducer can capture the biomechanical properties in different tissue areas. Some of the results are shown in Tables 1 and 2. From tables 1 and 2, one can observe the difference in the stiffness values obtained from the three sectors of the torsional wave probe. In table 1, the probe sector at 0º, that is, parallel to the fiber orientation of the breast fibers returns higher values of stiffness as expected. Results are encouraging; the anisotropic probe has been shown to be able to capture the tissue variability respect to the fiber orientation and frequency with a tendency close enough to the gold standard in elastography. This new technology can be considered as a baseline for future studies on TWE.

Objective 4: Non-linear shear elasticity

In this work, as a first contribution, we proposed a new hyperelastic model (nonlinear model) based on the Fourth Order Elastic Constants (FOECs) in the sense of Landau's theory to reconstruct the nonlinear parameters in cervical tissue by fitting the experimental data with this model. The experimetal data were also fitted by the most used hyperelastic models in the literature, Mooney–Rivlin, and Ogden. The nonlinear parameter A from the proposed model could be an important biomarker in connective cervical tissue diagnosis. As a second contribution, a comparison of the shear modulus, extracted from three different procedures, between the epithelial and connective layers of ex vivo cervical tissue was performed. The conclusion is that shear modulus was dependent on anatomical location of the cervical tissue. Despite the difficulties encountered in the characterization of the hyperelastic behaviour of cervical tissue, the proposed nonlinear model should be considered as the basis of more complex constitutive equations. Nevertheless, the nonlinear FOEC model should remain as the starting point in the hyperelastic characterization of the cervical tissue in future studies.

"One never notices what has been done; one can only see what remains to be done."

Marie Curie

Chapter6

Limitations and directions for the future

Future short-term work will explore new corneal and anisotropy sensor designs, with dimensions adapted to different types of samples. The ethical committee has been requested to perform in vivo measurements on the corneas of sedated animals. With these tests, we will explore the viability of the anisotropic sensor in vivo. Another of the lines started is to investigate the non-linearity of the cervix more deeply by sampling at different amplitudes and cycles and locating the harmonics and the adjustment with a numerical model. I will explore the possible relationship between the fractional alpha of fractional viscoelastic models and tissue vascularization (or fractality) within the coming months.

Bibliography

[1] Jorge Torres, Inas Faris, and Antonio Callejas. Histobiomechanical remodeling of the cervix during pregnancy: Proposed framework. *Mathematical Problems in Engineering*, 2019, 2019.

[2] Inas H Faris, Juan Melchor, Antonio Callejas, Jorge Torres, and Guillermo Rus. Viscoelastic biomarkers of ex vivo liver samples via torsional wave elastography. *Diagnostics*, 10(2):111, 2020.

[3] Antonio Callejas, Juan Melchor, Inas H Faris, and Guillermo Rus. Hyperelastic ex vivo cervical tissue mechanical characterization. *Sensors*, 20(16):4362, 2020.

[4] Gerhard A Holzapfel et al. Biomechanics of soft tissue. *The handbook of materials behavior models*, 3:1049–1063, 2001.

[5] Jay D Humphrey. Continuum biomechanics of soft biological tissues. *Proceedings of the Royal Society of London. Series A: Mathematical, Physical and Engineering Sciences*, 459(2029):3–46, 2003.

[6] Joy Y Vink, Sisi Qin, Clifton O Brock, Noelia M Zork, Feltovich Helen M, Xiaowei Chen, Urie Paul, Kristin M Myers, Timothy J Hall, Ronald Wapner, et al. A new paradigm for the role of smooth muscle cells in the human cervix. *American journal of obstetrics and gynecology*, 215(4):478–e1, 2016.

[7] Yoshida Kyoko, Mala Mahendroo, Joy Vink, Ronald Wapner, and Kristin Myers. Material properties of mouse cervical tissue in normal gestation. *Acta Biomaterialia*, 36:195–209, may 2016.

[8] Susan Tucker. Blackburn. *Parturition and uterine physiology. Maternal, fetal, & neonatal physiology : a clinical perspective.* Elsevier Saunders, 2013.

[9] Albert Singer and Joseph A. Jordan. The Functional Anatomy of the Cervix, the Cervical Epithelium and the Stroma (2009). In *The Cervix*, pages 13–37. Blackwell Publishing Ltd., Oxford, UK.

[10] Lorie M. Harper, Aaron B. Caughey, Anthony O. Odibo, Kimberly A. Roehl, Qiuhong Zhao, and Alison G. Cahill. Normal Progress of Induced Labor. *Obstetrics & Gynecology*, 119(6):1113–1118, jun 2012.

[11] Lindsey C Carlson, Stephanie T Romero, Palmeri Mark L, A Muñoz del Rio, Sean M Esplin, Rotemberg Veronica M, Timothy J Hall, and Feltovich Helen. Changes in shear wave speed pre-and post-induction of labor: a feasibility study. *Ultrasound in Obstetrics & Gynecology*, 46(1):93–98, 2015.

[12] Tristan Gauthier, Sophie Mazeau, François Dalmay, Eyraud Jean-Luc, Cyril Catalan, Benoit Marin, and Aubard Yves. Obesity and cervical ripening failure risk. *The Journal of Maternal-Fetal & Neonatal Medicine*, 25(3):304–307, mar 2012.

[13] Jacob R. Lassiter, Nicolette Holliday, David F. Lewis, Madhuri Mulekar, Abshire Jacob, and Brian Brocato. Induction of labor with an unfavorable cervix: how does BMI affect success? *The Journal of Maternal-Fetal & Neonatal Medicine*, pages 1–3, nov 2015.

[14] Read Charles P, Word R Ann, Monika A Ruscheinsky, Brenda C Timmons, and Mala S Mahendroo. Cervical remodeling during pregnancy and parturition: molecular characterization of the softening phase in mice. *Reproduction*, 134(2):327–340, aug 2007.

[15] S Y Yu, Tozzi C A, J Babiarz, and P C Leppert. Collagen changes in rat cervix in pregnancy–polarized light microscopic and electron microscopic studies. *Proceedings of the Society for Experimental Biology and Medicine. Society for Experimental Biology and Medicine (New York, N.Y.)*, 209(4):360–8, sep 1995.

[16] F G Cunningham, N F Gant, K J Leveno, L C Gilstrap 3rd, Hauth J C, and K D Wenstrom. General considerations and maternal evaluation. *Williams obstetrics*, pages 912–925, 2010.

[17] Cameron G. Barclay, Brennand Janet E., Rodney W. Kelly, and Andrew A. Galder. Interleukin-8 production by the human cervix. *American Journal of Obstetrics and Gynecology*, 169(3):625–632, sep 1993.

[18] E. El Maradny, Kanayama N., Kobayashi H., B. Hossain, S. Khatun, Liping S., Kobayashi T., and T. Terao. The role of hyaluronic acid as a mediator and regulator of cervical ripening. *Human Reproduction*, 12(5):1080–1088, may 1997.

[19] Mikitaka Obara, Hideto Hirano, Masaki Ogawa, Tsubaki Hiromitsu, Hosoya Naoko, Yoshida Yuko, Miyauchi Satoshi, and Tanaka Toshinobu. Changes in molecular weight of hyaluronan and hyaluronidase activity in uterine cervical mucus in cervical ripening. *Acta Obstetricia et Gynecologica Scandinavica*, 80(6):492–496, jan 2001.

[20] Catherine L Elliott, Brennand Janet E, and Andrew A Calder. The effects of mifepristone on cervical ripening and labor induction in primigravidae. *Obstetrics & Gynecology*, 92(5):804–809, nov 1998.

[21] Word R, Li Xiang-Hong, Michael Hnat, and Kelley Carrick. Dynamics of Cervical Remodeling during Pregnancy and Parturition: Mechanisms and Current Concepts. *Seminars in Reproductive Medicine*, 25(1):069–079, jan 2007.

[22] S. M. Yellon, A. M. Mackler, and M. A. Kirby. The Role of Leukocyte Traffic and Activation in Parturition. *Journal of the Society for Gynecologic Investigation*, 10(6):323–338, sep 2003.

[23] Kristin M. Myers, Feltovich Helen, Mazza Edoardo, Joy Vink, Bajka Michael, Ronald J. Wapner, Timothy J. Hall, and House Michael. The mechanical role of the cervix in pregnancy. *Journal of Biomechanics*, 48(9):1511–1523, jun 2015.

[24] Wang Yao, Yu Gan, Kristin M. Myers, Joy Y. Vink, Ronald J. Wapner, and Christine P. Hendon. Collagen Fiber Orientation and Dispersion in the Upper Cervix of Non-Pregnant and Pregnant Women. *PLOS ONE*, 11(11):e0166709, nov 2016.

[25] Kristin M Myers, Feltovich Helen, Mazza Edoardo, Joy Vink, Bajka Michael, Ronald J Wapner, Timothy J Hall, and House Michael. The mechanical role of the cervix in pregnancy. *Journal of biomechanics*, 48(9):1511–1523, 2015.

[26] V Dubrauszky. Further observations on the structure of the uterine wall during pregnancy]. *Archiv fur Gynakologie*, 202:41–3, 1965.

[27] House Michael, Bhadelia Rafeeque A., Kristin Myers, and Socrate Simona. Magnetic resonance imaging of three-dimensional cervical anatomy in the second and third trimester. *European Journal of Obstetrics & Gynecology and Reproductive Biology*, 144:S65–S69, may 2009.

[28] P C Leppert. Anatomy and physiology of cervical ripening. *Clinical obstetrics and gynecology*, 38(2):267–79, jun 1995.

[29] Ivan M Rosado-Mendez, Palmeri Mark L, Lindsey C Drehfal, Quinton W Guerrero, Heather Simmons, Feltovich Helen, and Timothy J Hall. Assessment of structural heterogeneity and viscosity in the cervix using shear wave elasticity imaging: initial results from a rhesus macaque model. *Ultrasound in medicine & biology*, 43(4):790–803, 2017.

[30] Wang Yao, Yoshida Kyoko, Michael Fernandez, Joy Vink, Ronald J Wapner, Ananth Cande V, Michelle L Oyen, and Kristin M Myers. Measuring the compressive viscoelastic mechanical properties of human cervical tissue using indentation. *Journal of the mechanical behavior of biomedical materials*, 34:18–26, 2014.

[31] Andrea R. Westervelt, Michael Fernandez, House Michael, Joy Vink, Nhan-Chang Chia-Ling, Ronald Wapner, and Kristin M. Myers. A Parameterized Ultrasound-Based Finite Element Analysis of the Mechanical Environment of Pregnancy. *Journal of Biomechanical Engineering*, 139(5):051004, apr 2017.

[32] M. Fernandez, House M., S. Jambawalikar, N. Zork, J. Vink, R. Wapner, and K. Myers. Investigating the mechanical function of the cervix during pregnancy using finite element models derived from high-resolution 3D MRI. *Computer Methods in Biomechanics and Biomedical Engineering*, 19(4):404–417, mar 2016.

[33] K J Parker, M M Doyley, and D J Rubens. Corrigendum: Imaging the elastic properties of tissue: the 20 year perspective. *Physics in Medicine and Biology*, 2012.

[34] J Ophir, I Ccspedes, Ponnekanti H, Yazdi Y, and Li X. ELASTOGRAPHY A QUANTITATIVE METHOD FOR IMAGING THE ELASTICITY OF BIOLOGICAL TISSUES. Technical report, 1991.

[35] Venkatesh Sudhakar K., Meng Yin, and Richard L. Ehman. Magnetic resonance elastography of liver: Technique, analysis, and clinical applications. *Journal of Magnetic Resonance Imaging*, 37(3):544–555, 2013.

[36] Lamiaa Mobarak, Mohammed M. Nabeel, Ehsan Hassan, Dalia Omran, and Zakaria Zeinab. Real-time elastography as a noninvasive assessment of liver fibrosis in chronic hepatitis C Egyptian patients: A prospective study. *Annals of Gastroenterology*, 2016.

[37] A. Thomas. Imaging of the cervix using sonoelastography. *Ultrasound in Obstetrics and Gynecology*, 2006.

[38] Anke Thomas, Sherko Kümmel, Ole Gemeinhardt, and Thomas Fischer. Real-Time Sonoelastography of the Cervix: Tissue Elasticity of the Normal and Abnormal Cervix. *Academic Radiology*, 2007.

[39] Molina FS, Gómez LF, Florido J, Padilla MC, and Nicolaides KH. Quantification of cervical elastography: a reproducibility study. *Ultrasound in Obstetrics & Gynecology*, 39(6):685–689, 2012.

[40] Hernandez-Andrade E., S. S. Hassan, H. Ahn, Korzeniewski S. J., L. Yeo, Chaiworapongsa T., and R. Romero. Evaluation of cervical stiffness during pregnancy using semiquantitative ultrasound elastography. *Ultrasound in Obstetrics and Gynecology*, 2013.

[41] Feltovich H. and T. J. Hall. Quantitative imaging of the cervix: setting the bar. *Ultrasound in Obstetrics & Gynecology*, 41(2):121–128, feb 2013.

[42] M. M. Maurer, S. Badir, Pensalfini M., Bajka M., Abitabile P., R. Zimmermann, and Mazza E. Challenging the in-vivo assessment of biomechanical properties of the uterine cervix: A critical analysis of ultrasound based quasi-static procedures. *Journal of Biomechanics*, 2015.

[43] A. Fruscalzo, R. Schmitz, Klockenbusch W., and Steinhard J. Reliability of cervix elastography in the late first and second trimester of pregnancy. *Ultraschall in der Medizin*, 2012.

[44] Hee Lene, Puk Sandager, Olav Petersen, and Uldbjerg Niels. Quantitative sonoelastography of the uterine cervix by interposition of a synthetic reference material. *Acta Obstetricia et Gynecologica Scandinavica*, 2013.

[45] Arrigo Fruscalzo, Ambrogio P. Londero, and Ralf Schmitz. Quantitative cervical elastography during pregnancy: influence of setting features on strain calculation. *Journal of Medical Ultrasonics*, 2015.

[46] A. Fruscalzo, A. P. Londero, Fröhlich C., U. Möllmann, and R. Schmitz. Quantitative elastography for cervical stiffness assessment during pregnancy. *BioMed Research International*, 2014.

[47] A. Fruscalzo, R. Schmitz, Klockenbusch W., and Steinhard J. Reliability of cervix elastography in the late first and second trimester of pregnancy. *Ultraschall in der Medizin*, 2012.

[48] Mazza Edoardo, Parra-Saavedra Miguel, Bajka Michael, Eduard Gratacos, Kypros Nicolaides, and Jan Deprest. <i>In vivo</i> assessment of the biomechanical properties of the uterine cervix in pregnancy. *Prenatal Diagnosis*, 34(1):33–41, jan 2014.

[49] Arrigo Fruscalzo, Mazza Edoardo, Feltovich Helen, and Ralf Schmitz. Cervical elastography during pregnancy: a critical review of current approaches with a focus on controversies and limitations. *Journal of Medical Ultrasonics*, 43(4):493–504, oct 2016.

[50] Robert M. Lerner, Huang S. R., and Kevin J. Parker. "Sonoelasticity" images derived from ultrasound signals in mechanically vibrated tissues. *Ultrasound in Medicine and Biology*, 1990.

[51] Mostafa Fatemi and James F. Greenleaf. Ultrasound-stimulated vibro-acoustic spectrography. *Science*, 280 5360:82–5, 1998.

[52] Laurent Sandrin, Mickaël Tanter, Catheline Stefan, and Mathias Fink. Shear modulus imaging with 2-d transient elastography. *IEEE transactions on ultrasonics, ferroelectrics, and frequency control*, 49(4):426–435, 2002.

[53] Brian J. Fahey, Kathryn Nightingale, R. C. Nelson, Mark L. Palmeri, and Gregg E. Trahey. Acoustic radiation force impulse imaging of the abdomen: demonstration of feasibility and utility. *Ultrasound in medicine & biology*, 31 9:1185–98, 2005.

[54] Kathryn Nightingale, Mark L. Palmeri, Roger W. Nightingale, and Gregg E. Trahey. On the feasibility of remote palpation using acoustic radiation force. *The Journal of the Acoustical Society of America*, 110 1:625–34, 2001.

[55] G. R. Torr. The acoustic radiation force. *American Journal of Physics*, 52(5):402–408, 1984.

[56] Wei Meng, Guangchen Zhang, Changjun Wu, Guozhu Wu, Yan Song, and Zhaoling Lu. Preliminary results of acoustic radiation force impulse (arfi) ultrasound imaging of breast lesions. *Ultrasound in medicine & biology*, 37 9:1436–43, 2011.

[57] Zhai Liang, John Madden, Wen-Chi Foo, Palmeri Mark L, Vladimir Mouraviev, Thomas J Polascik, and Nightingale Kathryn R. Acoustic radiation force impulse imaging of human prostates ex vivo. *Ultrasound Med. Biol.*, 36(4):576–588, 2010.

[58] Kathryn Nightingale, Stephen A. McAleavey, and Gregg E. Trahey. Shear-wave generation using acoustic radiation force: in vivo and ex vivo results. *Ultrasound in medicine & biology*, 29 12:1715–23, 2003.

[59] Jeffrey Bamber, Cosgrove D, Dietrich CF, J Fromageau, Bojunga J, Calliada F, Cantisani V, J-M Correas, M Donofrio, Drakonaki EE, et al. Efsumb guidelines and recommendations on the clinical use of ultrasound elastography. part 1: Basic principles and technology. *Ultraschall in der Medizin-European Journal of Ultrasound*, 34(02):169–184, 2013.

[60] Bercoff Jérémy, Mickael Tanter, and Mathias Fink. Supersonic shear imaging: a new technique for soft tissue elasticity mapping. *IEEE transactions on ultrasonics, ferroelectrics, and frequency control*, 51(4):396–409, 2004.

[61] J-L Gennisson, Thomas Deffieux, Mathias Fink, and Michaël Tanter. Ultrasound elastography: principles and techniques. *Diagnostic and interventional imaging*, 94(5):487–495, 2013.

[62] Armen P Sarvazyan, Oleg V Rudenko, Scott D Swanson, J.Brian Fowlkes, and Stanislav Y Emelianov. Shear wave elasticity imaging: a new ultrasonic technology of medical diagnostics. *Ultrasound in medicine & biology*, 24(9):1419 – 1435, 1998.

[63] Nightingale Kathryn, Palmeri Mark, and Gregg Trahey. Analysis of contrast in images generated with transient acoustic radiation force. *Ultrasound in Medicine and Biology*, 2006.

[64] Lindsey C. Carlson, Feltovich Helen, Palmeri Mark L., Alejandro Muñoz Del Rio, and Timothy J. Hall. Statistical analysis of shear wave speed in the uterine cervix. *IEEE Transactions on Ultrasonics, Ferroelectrics, and Frequency Control*, 2014.

[65] Lindsey C. Carlson, Helen Feltovich, Mark L. Palmeri, Jeremy J. Dahl, Alejandro Munoz del Rio, and Timothy J. Hall. Shear wave speed estimation in the human uterine cervix. *Ultrasound Obstet Gynecol*, 43:452–458, 2014.

[66] Marie Muller, Dora Aït-Belkacem, Hessabi Mahdieh, Jean-Luc Gennisson, Gilles Grangé, François Goffinet, Edouard Lecarpentier, Dominique Cabrol, Mickaël Tanter, and Vassilis Tsatsaris. Assessment of the cervix in pregnant women using shear wave elastography: a feasibility study. *Ultrasound in medicine & biology*, 41(11):2789–2797, 2015.

[67] Hernandez-Andrade Edgar, Alma Aurioles-Garibay, Garcia Maynor, Korzeniewski Steven J., Alyse G. Schwartz, Hyunyoung Ahn, Martinez-Varea Alicia, Lami Yeo, Chaiworapongsa Tinnakorn, Sonia S. Hassan, and Roberto Romero. Effect of depth on shear-wave elastography estimated in the internal and external cervical os during pregnancy. *Journal of Perinatal Medicine*, 2014.

[68] Lindsey C. Carlson, Timothy J. Hall, Ivan M. Rosado-Mendez, Mark L. Palmeri, and Helen Marcie Feltovich. Detection of changes in cervical softness using shear wave speed in early versus late pregnancy: An in vivo cross-sectional study. *Ultrasound in medicine & biology*, 44 3:515–521, 2017.

[69] Peralta L., G. Rus, Bochud N., and Molina F.S. Assessing viscoelasticity of shear wave propagation in cervical tissue by multiscale computational simulation. *Journal of Biomechanics*, 48(9):1549–1556, jun 2015.

[70] Hernandez-Andrade et al. Effect of depth on shear-wave elastography estimated in the internal and external cervical os during pregnancy. *J Perinat Med.*, 42(5):549–557, 2014.

[71] Marie Muller, Dora Aït-Belkacem, Mahdieh Hessabi, Jean luc Gennisson, Gilles Grange, F. Goffinet, Edouard R Lecarpentier, Dominique Cabrol, Mickaël Tanter, and Vassilis Tsatsaris. Assessment of the cervix in pregnant women using shear wave elastography: A feasibility study. *Ultrasound in medicine & biology*, 41 11:2789–97, 2015.

[72] Ivan M Rosado-Mendez, Lindsey C Carlson, Kaitlin M Woo, Andrew P Santoso, Quinton W Guerrero, Palmeri Mark L, Feltovich Helen, and Timothy J Hall. Quantitative assessment of cervical softening during pregnancy in the rhesus macaque with shear wave elasticity imaging. *Physics in Medicine & Biology*, 63(8):085016, 2018.

[73] M Fernandez, House M, S Jambawalikar, N Zork, J Vink, R Wapner, and K Myers. Investigating the mechanical function of the cervix during pregnancy using finite element models derived from high-resolution 3d mri. *Computer methods in biomechanics and biomedical engineering*, 19(4):404–417, 2016.

[74] K.M. Myers, Paskaleva A.P., House M., and Socrate S. Mechanical and biochemical properties of human cervical tissue. *Acta Biomaterialia*, 4(1):104–116, jan 2008.

[75] Blackburn Brecken J, Jenkins Michael W, Rollins Andrew M, and Dupps William J. A review of structural and biomechanical changes in the cornea in aging, disease, and photochemical crosslinking. *Frontiers in bioengineering and biotechnology*, 7:66, 2019.

[76] Singh Manmohan, Han Zhaolong, Li Jiasong, Vantipalli Srilatha, Aglyamov Salavat R, Twa Michael D, and Larin Kirill V. Quantifying the effects of hydration on corneal stiffness with noncontact optical coherence elastography. *Journal of Cataract & Refractive Surgery*, 44(8):1023–1031, 2018.

[77] Petsche Steven J, Chernyak Dimitri, Martiz Jaime, Levenston Marc E, and Pinsky Peter M. Depth-dependent transverse shear properties of the human corneal stroma. *Investigative ophthalmology & visual science*, 53(2):873–880, 2012.

[78] Hjortdal Jesper Ø. Regional elastic performance of the human cornea. *Journal of biomechanics*, 29(7):931–942, 1996.

[79] Binder Perry S. Ectasia after laser in situ keratomileusis. *Journal of Cataract & Refractive Surgery*, 29(12):2419–2429, 2003.

[80] Meek Keith M, Tuft Stephen J, Huang Yifei, Gill Paulvinder S, Hayes Sally, Newton Richard H, and Bron Anthony J. Changes in collagen orientation and distribution in keratoconus corneas. *Investigative ophthalmology & visual science*, 46(6):1948–1956, 2005.

[81] Cartwright Nathaniel E Knox, Tyrer John R, and Marshall John. Age-related differences in the elasticity of the human cornea. *Investigative ophthalmology & visual science*, 52(7):4324–4329, 2011.

[82] Wollensak Gregor, Spoerl Eberhard, and Seiler Theo. Riboflavin/ultraviolet-a–induced collagen crosslinking for the treatment of keratoconus. *American journal of ophthalmology*, 135(5):620–627, 2003.

[83] Meiri Zohar, Keren Shay, Rosenblatt Amir, Sarig Tal, Shenhav Liat, and Varssano David. Efficacy of corneal collagen cross-linking for the treatment of keratoconus: a systematic review and meta-analysis. *Cornea*, 35(3):417–428, 2016.

[84] Gonzalez-Andrades Miguel, Argüeso Pablo, and Gipson Ilene. Corneal anatomy. In *Corneal Regeneration*, pages 3–12. Springer, 2019.

[85] Meek Keith M and Knupp Carlo. Corneal structure and transparency. *Progress in retinal and eye research*, 49:1–16, 2015.

[86] Vinciguerra Riccardo, Ambrósio Jr Renato, Roberts Cynthia J, Azzolini Claudio, and Vinciguerra Paolo. Biomechanical characterization of subclinical keratoconus without topographic or tomographic abnormalities. *Journal of Refractive Surgery*, 33(6):399–407, 2017.

[87] Roy Abhijit Sinha, Shetty Rohit, and Kummelil Mathew Kurian. Keratoconus: a biomechanical perspective on loss of corneal stiffness. *Indian Journal of Ophthalmology*, 61(8):392, 2013.

[88] Antoine Ramier, Behrouz Tavakol, and Seok-Hyun Yun. Measuring mechanical wave speed, dispersion, and viscoelastic modulus of the cornea using optical coherence elastography. *Optics express*, 27(12):16635–16649, 2019.

[89] Han Zhaolong, Li Jiasong, Singh Manmohan, Wu Chen, Liu Chihhao, Raghunathan Raksha, Aglyamov Salavat R, Vantipalli Srilatha, Twa Michael D, and Larin Kirill V. Optical coherence elastography assessment of corneal viscoelasticity with a modified rayleigh-lamb wave model. *Journal of the mechanical behavior of biomedical materials*, 66:87–94, 2017.

[90] David Touboul, Jean-Luc Gennisson, Thu-Mai Nguyen, Antoine Robinet, Cynthia J Roberts, Mickael Tanter, and Nicolas Grenier. Supersonic shear wave elastography for the in vivo evaluation of transepithelial corneal collagen cross-linking. *Investigative ophthalmology & visual science*, 55(3):1976–1984, 2014.

[91] Thu-Mai Nguyen, Jean-Francois Aubry, Mathias Fink, Bercoff Jeremy, and Mickael Tanter. In vivo evidence of porcine cornea anisotropy using supersonic shear wave imaging. *Investigative ophthalmology & visual science*, 55(11):7545–7552, 2014.

[92] Mickaël Tanter, David Touboul, Jean-Luc Gennisson, Bercoff Jeremy, and Mathias Fink. High-resolution quantitative imaging of cornea elasticity using supersonic shear imaging. *IEEE transactions on medical imaging*, 28(12):1881–1893, 2009.

[93] Chen Pei-Yu, Shih Cho-Chiang, Lin Wei-Chen, Ma Teng, Zhou Qifa, Shung K Kirk, and Huang Chih-Chung. High-resolution shear wave imaging of the human cornea using a dual-element transducer. *Sensors*, 18(12):4244, 2018.

[94] Qian Xuejun, Ma Teng, Shih Cho-Chiang, Heur Martin, Zhang Jun, Shung Koping Kirk, Varma Rohit, Humayun Mark S, and Zhou Qifa.

Ultrasonic microelastography to assess biomechanical properties of the cornea. *IEEE Transactions on Biomedical Engineering*, 66(3):647–655, 2018.

[95] Couade Mathieu, Pernot Mathieu, Prada Claire, Messas Emmanuel, Emmerich Joseph, Bruneval Patrick, Criton Aline, Fink Mathias, and Tanter Mickael. Quantitative assessment of arterial wall biomechanical properties using shear wave imaging. *Ultrasound in medicine & biology*, 36(10):1662–1676, 2010.

[96] Mitchell A Kirby, Ivan Pelivanov, Song Shaozhen, Ambrozinski Lukasz, Soon Joon Yoon, Liang Gao, Li David, Tueng T Shen, Wang Ruikang K, and Matthew O'Donnell. Optical coherence elastography in ophthalmology. *Journal of biomedical optics*, 22(12):121720, 2017.

[97] Zaitsev Vladimir Y, Matveyev Alexander L, Matveev Lev A, Sovetsky Alexander A, Hepburn Matt S, Mowla Alireza, and Kennedy Brendan F. Strain and elasticity imaging in compression optical coherence elastography: The two-decade perspective and recent advances. *Journal of Biophotonics*, 14(2):e202000257, 2021.

[98] Matt S Hepburn, Wijesinghe Philip, Lixin Chin, and Brendan F Kennedy. Analysis of spatial resolution in phase-sensitive compression optical coherence elastography. *Biomedical optics express*, 10(3):1496–1513, 2019.

[99] Song Shaozhen, Wei Wei, Hsieh Bao-Yu, Ivan Pelivanov, Tueng T Shen, Matthew O'Donnell, and Wang Ruikang K. Strategies to improve phase-stability of ultrafast swept source optical coherence tomography for single shot imaging of transient mechanical waves at 16 khz frame rate. *Applied physics letters*, 108(19):191104, 2016.

[100] Abderrahmane Ouared, Emmanuel Montagnon, and Guy Cloutier. Generation of remote adaptive torsional shear waves with an octagonal phased array to enhance displacements and reduce variability of shear wave speeds: comparison with quasi-plane shear wavefronts. *Physics in medicine and biology*, 60 20:8161–85, 2015.

[101] S. R. Aglyamov, S. Park, Y. A. Ilinskii, and S. Y. Emelianov. Ultrasound imaging of soft tissue shear viscosity. In *IEEE Symposium on Ultrasonics, 2003*, volume 1, pages 937–940 Vol.1, 2003.

[102] INNITIUS Patent. Transductor ultrasónico de torsión para diagnóstico tisular. *Extensiones Internacionales, PCT/ES2012/070380*, 2011.

[103] INNITIUS Patent. Dispositivo emisor de ondas ultrasónicas de torsión y transductor que lo comprende. *Extensiones Internacionales, PCT/ES2016/070540*, 2015.

[104] Callejas Antonio, Gomez Antonio, Melchor Juan, Riveiro Miguel, Massó Paloma, Torres Jorge, López-López Modesto, and Rus Guillermo. Performance study of a torsional wave sensor and cervical tissue characterization. *Sensors*, 17(9):2078, 2017.

[105] Gennisson Jean-luc, Provost Jean, Deffieux Thomas, Papadacci Clément, Imbault Marion, Pernot Mathieu, and Tanter Mickael. 4-d ultrafast shear-wave imaging. *IEEE transactions on ultrasonics, ferroelectrics, and frequency control*, 62(6):1059–1065, 2015.

[106] Annin B.D. and Ostrosablin N.I. Anisotropy of elastic properties of materials. *Journal of Applied Mechanics and Technical Physics*, 49(6):998–1014, 2008.

[107] Atala Anthony, Kasper F Kurtis, and Mikos Antonios G. Engineering complex tissues. *Science translational medicine*, 4(160):160rv12–160rv12, 2012.

[108] James Casey and Marcel J Crochet. *Theoretical, Experimental, and Numerical Contributions to the Mechanics of Fluids and Solids: A collection of papers in honor of Paul M. Naghdi.* Birkhäuser, 2012.

[109] Robert S Langer and Vacanti Joseph P. Tissue engineering: the challenges ahead. *Scientific American*, 280(4):86–89, 1999.

[110] Simon Chatelin, Caroline Deck, and Rémy Willinger. An anisotropic viscous hyperelastic constitutive law for brain material finite-element modeling. *Journal of biorheology*, 27(1-2):26–37, 2013.

[111] Rachel B Groves, Sion A Coulman, James C Birchall, and Sam L Evans. An anisotropic, hyperelastic model for skin: experimental measurements, finite element modelling and identification of parameters for human and murine skin. *Journal of the mechanical behavior of biomedical materials*, 18:167–180, 2013.

[112] Grand Roman Joldes, Adam Wittek, and Karol Miller. Suite of finite element algorithms for accurate computation of soft tissue deformation for surgical simulation. *Medical image analysis*, 13(6):912–919, 2009.

[113] Taotao Wu, Alshareef Ahmed, Giudice J Sebastian, and Matthew B Panzer. Explicit modeling of white matter axonal fiber tracts in a

finite element brain model. *Annals of biomedical engineering*, pages 1–15, 2019.

[114] Bajka M and Haller U. Virtual reality based surgery simulation for endoscopic gynaecology. *Medicine Meets Virtual Reality: The Convergence of Physical & Informational Technologies: Options for a New Era in Healthcare*, 62:351, 1999.

[115] Yoshida Emilia A, Castro Márcia LA, and Martins Valéria F. Virtual reality and fetal medicine—a systematic review. In *2017 XLIII Latin American Computer Conference (CLEI)*, pages 1–10. IEEE, 2017.

[116] Misra Sarthak, Ramesh KT, and Okamura Allison M. Modeling of tool-tissue interactions for computer-based surgical simulation: a literature review. *Presence: Teleoperators and Virtual Environments*, 17(5):463–491, 2008.

[117] Lukasz Fracczak, Szaniewski Mateusz, and Podsedkowski Leszek. Share control of surgery robot master manipulator guiding tool along the standard path. *The International Journal of Medical Robotics and Computer Assisted Surgery*, 15(3):e1984, 2019.

[118] NA STEPHANE COTIN HERVE DELINGETTE. Efficient linear elastic models of soft tissues for real-time surgery simulation. Technical report, Tech. rep., Institut National de Recherche en Informoatique et en Automatique, 1998.

[119] Zhang Chenxi, Wang Manning, and Song Zhijian. A brain-deformation framework based on a linear elastic model and evaluation using clinical data. *IEEE Transactions on Biomedical Engineering*, 58(1):191–199, 2010.

[120] Fung Yuan-cheng. *Biomechanics: mechanical properties of living tissues*. Springer Science & Business Media, 2013.

[121] Veronda DR and RA Westmann. Mechanical characterization of skin—finite deformations. *Journal of biomechanics*, 3(1):111–124, 1970.

[122] Fung YC. Elasticity of soft tissues in simple elongation. *American Journal of Physiology-Legacy Content*, 213(6):1532–1544, 1967.

[123] Wex Cora, Arndt Susann, Stoll Anke, Bruns Christiane, and Kupriyanova Yuliya. Isotropic incompressible hyperelastic models for modelling the mechanical behaviour of biological tissues: a review. *Biomedical Engineering/Biomedizinische Technik*, 60(6):577–592, 2015.

[124] M Kohandel, S Sivaloganathan, Tenti G, and Drake JM. The constitutive properties of the brain parenchyma: Part 1. strain energy approach. *Medical engineering & physics*, 28(5):449–454, 2006.

[125] Rashid Badar, Destrade Michel, and Michael D Gilchrist. Mechanical characterization of brain tissue in simple shear at dynamic strain rates. *Journal of the mechanical behavior of biomedical materials*, 28:71–85, 2013.

[126] Zhan Gao and Desai Jaydev P. Estimating zero-strain states of very soft tissue under gravity loading using digital image correlation. *Medical image analysis*, 14(2):126–137, 2010.

[127] Yuan-Chiao Lu, Andrew R Kemper, and Costin D Untaroiu. Effect of storage on tensile material properties of bovine liver. *Journal of the mechanical behavior of biomedical materials*, 29:339–349, 2014.

[128] Costin D Untaroiu and Yuan-Chiao Lu. Material characterization of liver parenchyma using specimen-specific finite element models. *Journal of the mechanical behavior of biomedical materials*, 26:11–22, 2013.

[129] Baah-Dwomoh Adwoa, McGuire Jeffrey, Tan Ting, and De Vita Raffaella. Mechanical properties of female reproductive organs and supporting connective tissues: a review of the current state of knowledge. *Applied Mechanics Reviews*, 68(6), 2016.

[130] Barnum Carrie E, Fey Jennifer L, Weiss Stephanie N, Barila Guillermo, Brown Amy G, Connizzo Brianne K, Shetye Snehal S, Elovitz Michal A, and Soslowsky Louis J. Tensile mechanical properties and dynamic collagen fiber re-alignment of the murine cervix are dramatically altered throughout pregnancy. *Journal of biomechanical engineering*, 139(6), 2017.

[131] Myers Kristin M, Paskaleva AP, House Michael, and Socrate Simona. Mechanical and biochemical properties of human cervical tissue. *Acta biomaterialia*, 4(1):104–116, 2008.

[132] Michael J Poellmann, Edward K Chien, Barbara L McFarlin, and Amy J Wagoner Johnson. Mechanical and structural changes of the rat cervix in late-stage pregnancy. *Journal of the mechanical behavior of biomedical materials*, 17:66–75, 2013.

[133] Yoshida Kyoko, Mahendroo Mala, Vink Joy, Wapner Ronald, and Myers Kristin. Material properties of mouse cervical tissue in normal gestation. *Acta biomaterialia*, 36:195–209, 2016.

[134] Barone William R, Feola Andrew J, Moalli Pamela A, and Abramowitch Steven D. The effect of pregnancy and postpartum recovery on the viscoelastic behavior of the rat cervix. *Journal of mechanics in medicine and biology*, 12(01):1250009, 2012.

[135] Myers Kristin M, Socrate Simona, Paskaleva Anastassia, and House Michael. A study of the anisotropy and tension/compression behavior of human cervical tissue. *Journal of biomechanical engineering*, 132(2):021003, 2010.

[136] Jayyosi C, Lee N, A Willcockson, S Nallasamy, M Mahendroo, and K Myers. The mechanical response of the mouse cervix to tensile cyclic loading in term and preterm pregnancy. *Acta biomaterialia*, 78:308–319, 2018.

[137] Joseph Jordan, Albert Singer, Howard Jones, and Shafi Mahmood. *The cervix*. John Wiley & Sons, 2009.

[138] House Michael, David L Kaplan, and Socrate Simona. Relationships between mechanical properties and extracellular matrix constituents of the cervical stroma during pregnancy. In *Seminars in perinatology*, volume 33, pages 300–307. Elsevier, 2009.

[139] Phyllis C Leppert. Anatomy and physiology of cervical ripening. *Clinical obstetrics and gynecology*, 38(2):267–279, 1995.

[140] Jorge Torres, Inas Faris, and Antonio Callejas. Histobiomechanical remodeling of the cervix during pregnancy: proposed framework. *Mathematical Problems in Engineering*, vol(no):000–001, 2019.

[141] Kristin Myers, Socrate Simona, Dimitrios Tzeranis, and House Michael. Changes in the biochemical constituents and morphologic appearance of the human cervical stroma during pregnancy. *European Journal of Obstetrics & Gynecology and Reproductive Biology*, 144:S82–S89, 2009.

[142] Zork Noelia M, Myers Kristin M, Yoshida Kyoko, Cremers Serge, Jiang Hongfeng, Ananth Cande V, Wapner Ronald J, Kitajewski Jan, and Vink Joy. A systematic evaluation of collagen cross-links in the human cervix. *American journal of obstetrics and gynecology*, 212(3):321–e1, 2015.

[143] Elaine Nicpon Marieb and Katja Hoehn. *Human anatomy & physiology*. Pearson Education, 2007.

[144] Natali Arturo N, Emanuele L Carniel, and Hans Gregersen. Biomechanical behaviour of oesophageal tissues: material and structural configuration, experimental data and constitutive analysis. *Medical engineering & physics*, 31(9):1056–1062, 2009.

[145] Massó Paloma, Callejas Antonio, Melchor Juan, Molina Francisca S, and Rus Guillermo. In vivo measurement of cervical elasticity on pregnant women by torsional wave technique: A preliminary study. *Sensors*, 19(15):3249, 2019.

[146] Rus Guillermo, Muñoz Rafael, Melchor Juan, Molina Ruben, Callejas Antonio, Riveiro Miguel, Massó Paloma, Torres Jorge, Moreu Gerardo, Molina Francisca, et al. Torsion ultrasonic sensor for tissue mechanical characterization. In *2016 IEEE International Ultrasonics Symposium (IUS)*, pages 1–4. IEEE, 2016.

[147] Callejas Antonio, Gomez Antonio, Faris Inas H, Melchor Juan, and Rus Guillermo. Kelvin–voigt parameters reconstruction of cervical tissue-mimicking phantoms using torsional wave elastography. *Sensors*, 19(15):3281, 2019.

[148] LD Landau and EM Lifshitz. Elasticity theory. 1975.

[149] Hamilton Mark F, Ilinskii Yurii A, and Zabolotskaya Evgenia A. Separation of compressibility and shear deformation in the elastic energy density (l). *The Journal of the Acoustical Society of America*, 116(1):41–44, 2004.

[150] Destrade Michel and Raymond W Ogden. On the third-and fourth-order constants of incompressible isotropic elasticity. *The Journal of the Acoustical Society of America*, 128(6):3334–3343, 2010.

[151] A Cemal Eringen and Suhubi ES. Nonlinear theory of simple micro-elastic solids. *International Journal of Engineering Science*, 2(2):189–203, 1964.

[152] Rafael Muñoz and Juan Melchor. Nonlinear classical elasticity model for materials with fluid and matrix phases. *Mathematical Problems in Engineering*, 2018, 2018.

[153] Melvin Mooney. A theory of large elastic deformation. *Journal of applied physics*, 11(9):582–592, 1940.

[154] RS Rivlin. Large elastic deformations of isotropic materials iv. further developments of the general theory. *Philosophical Transactions*

of the Royal Society of London. Series A, Mathematical and Physical Sciences, 241(835):379–397, 1948.

[155] Martins PALS, Natal Jorge RM, and Ferreira AJM. A comparative study of several material models for prediction of hyperelastic properties: Application to silicone-rubber and soft tissues. *Strain*, 42(3):135–147, 2006.

[156] Raymond William Ogden. Large deformation isotropic elasticity–on the correlation of theory and experiment for incompressible rubberlike solids. *Proceedings of the Royal Society of London. A. Mathematical and Physical Sciences*, 326(1567):565–584, 1972.

[157] Juan Manuel Melchor and Guillermo Rus. Torsional ultrasonic transducer computational design optimization. *Ultrasonics*, 54 7:1950–62, 2014.

[158] Melchor Juan, Muñoz Rafael, and Guillermo Rus. Torsional ultrasound sensor optimization for soft tissue characterization. *Sensors*, 17(6):1402, 2017.

[159] Jeremy Bercoff, Mickaex0308l Tanter, and M K Fink. Supersonic shear imaging: a new technique for soft tissue elasticity mapping. *IEEE Transactions on Ultrasonics, Ferroelectrics and Frequency Control*, 51:396–409, 2004.

[160] Deng Yufeng, Rouze Ned C, Palmeri Mark L, and Nightingale Kathryn R. Ultrasonic shear wave elasticity imaging sequencing and data processing using a verasonics research scanner. *IEEE transactions on ultrasonics, ferroelectrics, and frequency control*, 64(1):164–176, 2016.

[161] Mark L. Palmeri, Stephen A. McAleavey, Gregg E. Trahey, and Kathryn Nightingale. Ultrasonic tracking of acoustic radiation force-induced displacements in homogeneous media. *IEEE Transactions on Ultrasonics, Ferroelectrics and Frequency Control*, 53:1300–1313, 2006.

[162] Thomas Deffieux, Jean luc Gennisson, Benoît Larrat, Maximilian Fink, and Mickaël Tanter. The variance of quantitative estimates in shear wave imaging: Theory and experiments. *IEEE Transactions on Ultrasonics, Ferroelectrics and Frequency Control*, 59, 2012.

[163] José M. Carcione, editor. *Wave Fields in Real Media (Third Edition)*. Elsevier, third edition edition, 2015.

[164] Laura Peralta. *Feasibility of using ultrasonic shear waves to assess cervical remodelling during the gestation period.* PhD thesis, Departamento de Mecánica Estructural e Ingeniería Hidráulica, University of Granada, May 2015.

[165] Stefan Catheline, Jean luc Gennisson, Giles Delon, Mathias Fink, Ralph Sinkus, Saïd Abouelkaram, and Joseph Culioli. Measuring of viscoelastic properties of homogeneous soft solid using transient elastography: an inverse problem approach. *The Journal of the Acoustical Society of America*, 116 6:3734–41, 2004.

[166] Thanasis Loupas, J. Powers, and R. W. Gill. An axial velocity estimator for ultrasound blood flow imaging, based on a full evaluation of the doppler equation by means of a two-dimensional autocorrelation approach. *IEEE Transactions on Ultrasonics, Ferroelectrics and Frequency Control*, 42:672–688, 1995.

[167] Alfonso Rodriguez-Molares, Ole Marius Hoel Rindal, Olivier Bernard, Hervé Liebgott, Andreas Austeng, and Lasse Lovstakken. The ultrasound toolbox. *2017 IEEE International Ultrasonics Symposium (IUS)*, pages 1–1, 2017.

[168] Mansouri MR and Darijani H. Constitutive modeling of isotropic hyperelastic materials in an exponential framework using a self-contained approach. *International Journal of Solids and Structures*, 51(25-26):4316–4326, 2014.

[169] Richard M Aspden. Collagen organisation in the cervix and its relation to mechanical function. *Collagen and related research*, 8(2):103–112, 1988.

[170] Patalano Antoine, García Carlos Marcelo, and Rodríguez Andrés. Rectification of image velocity results (river): a simple and user-friendly toolbox for large scale water surface particle image velocimetry (piv) and particle tracking velocimetry (ptv). *Computers & Geosciences*, 109:323–330, 2017.

[171] Patalano A, Garcia CM, Brevis W, Bleninger T, Guillen N, Moreno L, and Rodriguez A. Recent advances in eulerian and lagragian large-scale particle image velocimetry. In *E-proceedings of the 36th IAHR World Congress, The Hauge, Netherlands*, 2015.

[172] Marko B. Orescanin, Muqeem A. Qayyum, Kathleen S. Toohey, and Michael F. Insana. Complex shear modulus of thermally-damaged

liver. *2009 IEEE International Ultrasonics Symposium*, pages 127–130, 2009.

[173] Christopher Taylor Barry, Bradley Jay Mills, Zaegyoo Hah, Robert A Mooney, Charlotte Kathryn Ryan, Deborah J. Rubens, and Kevin J. Parker. Shear wave dispersion measures liver steatosis. *Ultrasound in medicine & biology*, 38 2:175–82, 2012.

[174] Seong-Ook Kim, Sang-Yun Lee, So-Ick Jang, Soo jin Park, Hye-Won Kwon, Seong-Ho Kim, Chin Siong Lee, Eun-Seok Choi, Seong-Kyu Cho, Sun Hwa Hong, and Yang-Min Kim. Hepatic stiffness using shear wave elastography and the related factors for a fontan circulation. *Pediatric Cardiology*, 39:57–65, 2017.

[175] Xuan Zhou Ding, Debaditya Dutta, Ahmed Mustafa Mahmoud, Bryan W. Tillman, Steven A. Leers, and Kang Kim. An adaptive displacement estimation algorithm for improved reconstruction of thermal strain. *IEEE Transactions on Ultrasonics, Ferroelectrics, and Frequency Control*, 62:138–151, 2015.

[176] Gianmarco Pinton, Jeremy J. Dahl, and Gregg E. Trahey. Rapid tracking of small displacements with ultrasound. *IEEE Transactions on Ultrasonics, Ferroelectrics and Frequency Control*, 53:1103–1117, 2006.

[177] M. Fink, L. Sandrin, M. Tanter, S. Catheline, S. Chaffai, J. Bercoff, and J. Gennisson. Ultra high speed imaging of elasticity. In *2002 IEEE Ultrasonics Symposium, 2002. Proceedings.*, volume 2, pages 1811–1820 vol.2, Oct 2002.

[178] Rosa M.S. Sigrist, Joy Liau, Ahmed El Kaffas, Maria Cristina Chammas, and Juergen K. Willmann. Ultrasound elastography: Review of techniques and clinical applications. In *Theranostics*, 2017.

[179] Eun Kyoung Hong, Young Hun Choi, Jung Eun Cheon, Woo Sun Kim, In-One Kim, and Sun Young Kang. Accurate measurements of liver stiffness using shear wave elastography in children and young adults and the role of the stability index. In *Ultrasonography*, 2017.

[180] Anthony E. Samir and Manish Dhyani et al. Shear-wave elastography for the estimation of liver fibrosis in chronic liver disease: determining accuracy and ideal site for measurement. *Radiology*, 274 3:888–96, 2015.

[181] Anesa Mulabecirovic, Anders Batman Mjelle, Odd Helge Gilja, Mette Vesterhus, and Roald Flesland Havre. Repeatability of shear wave

elastography in liver fibrosis phantoms—evaluation of five different systems. In *PloS one*, 2018.

[182] C F Dietrich and Jeffrey Bamber et al. Efsumb guidelines and recommendations on the clinical use of liver ultrasound elastography, update 2017 (long version). *Ultraschall in der Medizin*, 38 4:e48, 2017.

[183] Mireen Friedrich-Rust, Thierry Poynard, and Laurent Castera. Critical comparison of elastography methods to assess chronic liver disease. *Nature Reviews Gastroenterology & Hepatology*, 13:402–411, 2016.

[184] Thomas Deffieux and Jean luc Gennisson et al. Investigating liver stiffness and viscosity for fibrosis, steatosis and activity staging using shear wave elastography. *Journal of hepatology*, 62 2:317–24, 2015.

[185] Najat Salameh and Benoît Larrat et al. Early detection of steatohepatitis in fatty rat liver by using mr elastography. *Radiology*, 253 1:90–7, 2009.

[186] Marie Muller, Jean-Luc Gennisson, Thomas Deffieux, Mickaël Tanter, and Mathias Fink. Quantitative viscoelasticity mapping of human liver using supersonic shear imaging: preliminary in vivo feasibility study. *Ultrasound in medicine & biology*, 35 2:219–29, 2009.

[187] Changtian Li, Changsheng Zhang, Jun lai Li, Huiping Huo, and Danfei Song. Diagnostic accuracy of real-time shear wave elastography for staging of liver fibrosis: A meta-analysis. *Medical science monitor : international medical journal of experimental and clinical research*, 22:1349–59, 2016.

[188] Bruno Lapuyade et al Christophe Cassinotto. Non-invasive assessment of liver fibrosis with impulse elastography: comparison of supersonic shear imaging with arfi and fibroscan®. *Journal of hepatology*, 61 3:550–7, 2014.

[189] Chen Shigao, Sanchez William, Callstrom Matthew R, Gorman Brian, Lewis Jason T, Sanderson Schuyler O, Greenleaf James F, Xie Hua, Shi Yan, Pashley Michael, et al. Assessment of liver viscoelasticity by using shear waves induced by ultrasound radiation force. *Radiology*, 266(3):964–970, 2013.

[190] Deffieux Thomas, Montaldo Gabriel, Tanter Mickaël, and Fink Mathias. Shear wave spectroscopy for in vivo quantification of human soft tissues visco-elasticity. *IEEE transactions on medical imaging*, 28(3):313–322, 2008.

[191] Bercoff Jérémy, Tanter Mickaël, Muller Marie, and Fink Mathias. The role of viscosity in the impulse diffraction field of elastic waves induced by the acoustic radiation force. *IEEE transactions on ultrasonics, ferroelectrics, and frequency control*, 51(11):1523–1536, 2004.

[192] Barry Christopher T, Hah Zaegyoo, Partin Alexander, Mooney Robert A, Chuang Kuang-Hsiang, Augustine Alicia, Almudevar Anthony, Cao Wenqing, Rubens Deborah J, and Parker Kevin J. Mouse liver dispersion for the diagnosis of early-stage fatty liver disease: A 70-sample study. *Ultrasound in medicine & biology*, 40(4):704–713, 2014.

[193] Callejas Zafra Antonio Manuel et al. Feasibility of using torsional waves to assess viscoelasticity of cervical tissue. 2019.